

Article

A Comparison of a Transparent Thermal Insulation System Filled with Refrigerants and a Pig-Fat Based PCM

Agustín Torres Rodríguez ^{1,*}, David Morillón Gálvez ², Iván García Kerdan ³ and Rodolfo Silva Casarín ²¹ Posgrado de Arquitectura, Universidad Nacional Autónoma de México, Mexico City 04510, Mexico² Instituto de Ingeniería, Universidad Nacional Autónoma de México, Mexico City 04510, Mexico; damg@pumas.iingen.unam.mx (D.M.G.); rsilvac@iingen.unam.mx (R.S.C.)³ Tecnológico de Monterrey, School of Engineering and Sciences, Mexico City 01389, Mexico; i.garciakerdan@tec.mx

* Correspondence: agustin.torres@enp.unam.mx

Abstract: In this research sustainable refrigerants are tested as filler gases in Transparent Thermal Insulation (TTI) for the first time. These are compared with pig fat, a readily available material with good thermal inertia that is proposed as an organic phase change material (PCM). The aim of this paper is to compare the thermal behaviour of a Hybrid Air Conditioning System (HACS) with TTI filled with R134a, R1233zd and a pig-fat-based PCM. Numerical simulations using the OPAQUE 3 program and two online platforms are used to evaluate the possible application of TTI and PCM as passive systems. Additionally, three TTI models are used to simulate the heat transfer processes of TTI, PCM and R134a. The velocity of the flow in the air gap is also analysed numerically in both laminar and turbulent states. For the assessment, infrared thermographic imagery is used to measure the temperatures in the HACS, giving values of 46.17 °C by day and 38.05 °C at night. The results show that the heat loss and heat gain in the combination TTI filled with refrigerants and pig-fat-based PCM are between 2.22 and 1.51 W/m². In addition, the HACS was able to keep a small box warm during the night. The flow in the air gap of the HACS can be controlled by installing Ni-Ti wire actuators with a cooling temperature of 23 °C and a heating temperature of 70 °C. The Ni-Ti wire actuators can open and close the dampers at 23 °C and 51 °C, respectively. By installing a 5-watt solar-power fan, the velocity of the flow in the air gap in the HACS can be increased, thus improving the efficiency of the system. In all the experiments, the pig fat proved to be suitable for use in building applications as a non-flammable organic material.

Keywords: hybrid air conditioning system; transparent thermal insulation; infrared thermography; refrigerant; phase change material



Citation: Torres Rodríguez, A.; Morillón Gálvez, D.; García Kerdan, I.; Silva Casarín, R. A Comparison of a Transparent Thermal Insulation System Filled with Refrigerants and a Pig-Fat Based PCM. *Energies* **2023**, *16*, 3630. <https://doi.org/10.3390/en16093630>

Academic Editors: Xin Min, Xiaoguang Zhang and Nianben Zheng

Received: 17 March 2023

Revised: 18 April 2023

Accepted: 19 April 2023

Published: 23 April 2023



Copyright: © 2023 by the authors. Licensee MDPI, Basel, Switzerland. This article is an open access article distributed under the terms and conditions of the Creative Commons Attribution (CC BY) license (<https://creativecommons.org/licenses/by/4.0/>).

1. Introduction

In residential and commercial buildings, heating, ventilation and air-conditioning (HVAC) systems control the temperature, humidity, velocity and filtration of indoor air. It is estimated that the electricity and gas consumption in buildings around the world will rise to nearly 2800 TWh by 2030, which is approximately the equivalent of present electricity demand in China [1]. Recent advances in compressors and refrigerants have reduced the demand for electricity in HVAC systems, but their sophisticated control systems, such as Building Management Systems (BMS) and Supervisory Control and Data Acquisition, still require considerable amounts of energy.

In order to make a correct diagnosis and elaborate solutions of environmental thermal conditions in buildings, several monitoring techniques have been used. Thermal imaging technology is a non-invasive means of measuring many points of an object at the same time by converting radiation energy into temperature information. Images are produced of the thermal patterns and anomalies of the object in an electromagnetic spectrum of infrared

light. Infrared image technology is widely used to detect the absence of insulation, or thermally defective insulation, in houses and buildings.

Infrared thermographic imagery is also used to evaluate the thermal behaviour of buildings, including the overall heat-transfer coefficient, or U-Value; that is, how well heat is conducted through conductive and convective barriers. The U-Value is the inverse of the total thermal resistance of plane wall, subject to convection on both sides. The U-Value and heat transfer through transparent thermal insulation of the Hybrid Air Conditioning System (HACS) can be computed with the measurement of temperatures with a data logger and infrared thermography [2].

Images from infrared thermographic equipment have been used to measure thermal bridges and detect areas of excessive heat loss, as well as to characterise the thermal efficiency of glazing and windows, and to detect moisture in walls [3]. Infrared thermographic imagery was used to estimate the temperature of the thermal insulation of exterior walls in a school near Paris in order to estimate the thermal insulation of the building's exterior walls [4].

Recent research has shown that while a new combination of phase change material and metal grains, known as micro-phase change material (MPCM), has good thermal conductivity, the microencapsulation process used to increase the heat transfer by conduction of PCM is the most expensive of all heat-storage methods. It has also been seen that the metallic structures are meticulously planned, so as to increase the thermal conductivity of the MPCM without decreasing their thermal storage capacity [5]. To reduce the costs of microencapsulation, pig fat was proposed as the phase change material (PCM) of the HACS in which the thermal behaviour was to be evaluated.

An HACS is the combination of parts of a passive system with HVAC system devices. Transparent Thermal Insulation (TTI) is a combination of translucent and opaque materials which may contain gases with low thermal conductivity, and that can capture and retain solar heat energy by minimising heat losses. The HACS has a TTI filled with refrigerants, to increase heat gain during the day and reduce heat loss at night in rooms where the system is installed.

TTI were first introduced in Europe in the 1980s, mainly in the facades of buildings, in order to reduce heat losses. Using Computational Fluid Dynamic (CFD) and experimental methods, recent research has shown the advantages of using TTI in energy-saving window systems. TTI double-glazing units with integrated parallel louvered TTI of different cell aspect ratios were analysed, showing a 35–46% reduction in thermal conductivity compared to double glazing without TTI [6].

In 2019, researchers investigated the thermal behaviour of TTI (glass X crystal) that had a thickness of 0.079 m and U-value of $0.48 \text{ W/m}^2 \text{ K}$. This system consists of safety glass 1; a cavity filled with transparent prismatic plate and inert gas; a sheet of safety glass 2; then a cavity filled with inert glass; a sheet of safety glass 3; a cavity of phase change material; and, finally, a sheet of safety glass 4. The TTI-PCM system is affected by factors such as thickness and U-value because the combination of these technologies uses aerogel, which has low thermal conductivity and good solar transmittance, and a wall with lower U-value and nominal thickness has few heat losses [7]. Other experimental and numerical studies have shown that TTI could reduce the very high heat losses during sunless periods and at night. The combination of TTI filled with gas with the lowest thermal conductivity and an organic PCM with good thermal inertia has the capacity to store passive solar energy and increase the heat gains [8–13].

The main advantages of the combination TTI filled with refrigerants and PCM, and its use with other passive solar techniques such as a Trombe wall, can be discussed. Next, advantages can be defined.

1. The Trombe wall and PCM will reduce the amount of energy consumed in the building, as the ventilated facade significantly improves the thermal behaviour of the exterior wall. During the day, the exterior wall is heated by solar radiation and the PCM melts; then at night, when the outdoor temperature falls below the phase change

temperature, the heat stored by the PCM is released and the air inside the building heats up.

2. The effective technology used on the façade exposed to solar radiation, such as natural ventilation, Prisma solar glass and shading devices, prevents overheating of the air inside of the building in summer and conserves the heat from the combined TTI-PCM and Trombe wall in winter [14].
3. The TTI-PCM and Trombe wall combination can be used as a passive heating system because the TTI can be filled with refrigerant 134a, which has similar thermal conductivity to noble gases such as krypton. (Krypton: 0.0094 W/m K at 25 °C and pressure 0.1 MPa. R134a: 0.01409 W/m K at 29.85 °C and pressure 0.122 MPa.) [15,16].
4. The transparent sheet used must be of a material such as acrylic, as the refrigerant expands when exposed to solar radiation. The sheet must be sufficiently flexible to withstand the increase in the volume of the refrigerant as its temperature rises. Many other works have found disadvantages of TTI-PCM systems, including:
 1. The highest fluxes occur in the pure liquid state of the PCM, which for PCM depends on the solar radiation, the size of the glazed area and the dimensions of ventilated façade [9].
 2. In a cold climate, the optimum area of the TTI-PCM wall must be increased, to allow more of the incident solar radiation to heat it [17].
 3. With more incident solar radiation, and a Trombe wall in the TTI-PCM, the building will overheat in summer. This can also occur when a large amount of refrigerant is used, such as transparent thermal material [14].

In this paper the degradation of pig fat properties was not investigated and this should be addressed in future experimental work.

This paper aims to evaluate the thermal behaviour of an HACS using TTI filled with R134a and R1233zd in combination with a pig-fat-based PCM. This was analysed in the heating of a small space of an HACS, overnight, in part of November and December, 2021. Another combination of the TTI filled with R1233zd and a pig-fat-based PCM was analysed in cooling mode for the same space, during the day, from January to April, 2022. The experiments were carried out in real conditions, with the HACS on a house roof in Nezahualcoyotl City, a suburb of the Greater Mexico City Metropolitan Area. A thermal imaging camera was used to show the behaviour of the HACS during the day and night. Additionally, a thermal study was made to calculate the U-value and heat loss of the TTI-PCM and compared with the results of three simulation runs with the Opaque program. A 3D model of the HACS was also made, and several CFD simulations were made to evaluate the heat-transfer process, to understand the flow velocities in the air gap and the thermal efficiency of R134a.

It is expected that the results of this research will be of use in the design of better exterior walls that not only serve as thermal insulation but also in passive ventilation and air-conditioning systems in buildings.

2. Materials and Methods

An experimental prototype of the HACS was built with the aim of evaluating the thermal behaviour of the TTI filled with R134a and later filled with R1233zd. A pig-fat-based PCM was also inserted into the HACS in order to complete the thermal evaluation at night. The study was carried out on the second-floor roof of a house in Nezahualcoyotl, Mexico in various months of the years 2020, 2021 and 2022.

2.1. Building the HACS

The HACS was designed facing south and receiving solar radiation on average between 6:50 h and 19:30 h. A plane mirror and a solar reflector plate reflected solar radiation towards the TTI during the day. Adjacent to the HACS was a small box with a volume of one cubic metre. The aim was to measure the temperature and velocity of the air gap that heated the TTI. The adjacent box was made of gypsum board, with a thickness of 16 mm,

and insulated with polyurethane of 2.54 mm. In the cooling mode, the upper damper was closed, the wind flowed across the slots of the linear diffuser and lower damper; it mixed with air inside the adjacent box and finally left by the top linear diffuser. In the heating mode, wind mixed with air inside the box, where the wind was heated up and flowed inside the channel of the TTI and PCM towards the upper damper, while the top linear diffuser was closed with polyurethane strips. The steps showing how the HACS was built can be seen in Appendix A. Figure 1 shows the set-up of the experiment on the rooftop, taken on 1 February 2023.

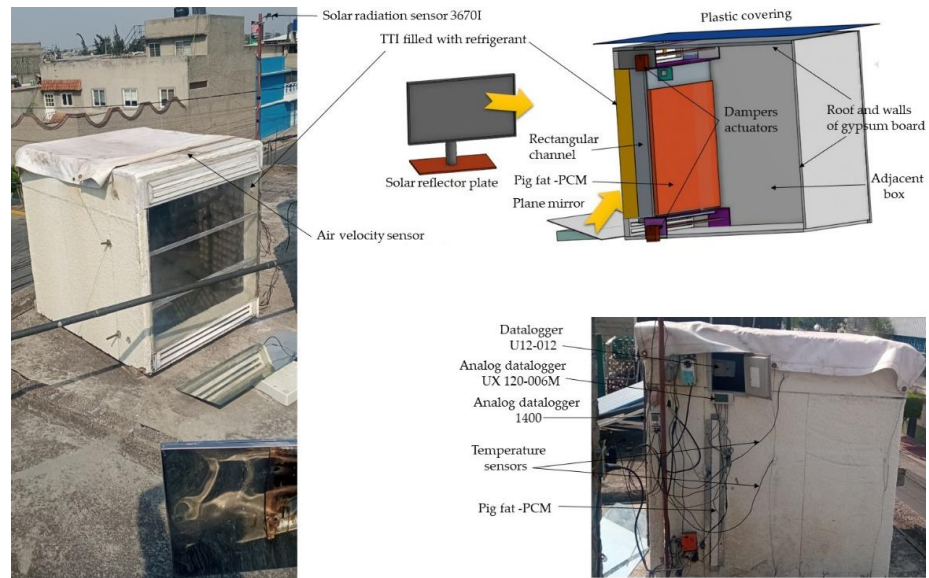


Figure 1. View of the HACS.

During experimentation, the air flowing inside the HACS through the gap moved very slowly. The air velocity sensor T-DCI-F300-1A3 was connected to the analogue data logger UX120-006 M to record the velocity of the air flowing inside the HACS in the heating mode. The air velocity sensor has a range of measurement of 0.15–1.00 m/s and can be used in corrosive and alkaline environments. To download the data into the computer, HOBOWare Pro 3.7.21 was used. Gray silicon was used to prevent rain entering the HACS at the point of connection of the sensor. Figure 2 shows a diagram of the air velocity sensor connection.

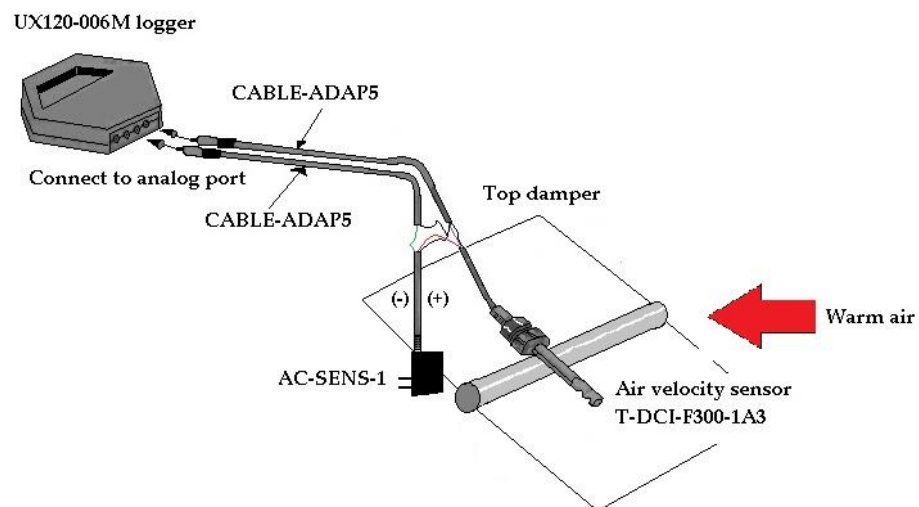


Figure 2. Air velocity sensor connection.

2.2. Recording the Behaviour of the TTIs

A range of devices was installed in the HACS to measure the temperature and flow velocity at the air gap, the pressure of the refrigerant in the TTI and the air temperature inside the adjacent box that was heated with PCM-based pig fat. Two dampers of gauge-24 galvanized-steel sheet were placed above and below the TTI position to control the airflow in and out of the HACS. Two linear diffusers with two slots allowed the heated air from the air gap and adjacent box to escape horizontally in almost any wind condition. A 9W lamp, placed in square polystyrene in the metal frame of the small window, was used to illuminate the TTI at night. A solar reflector and plane mirror were installed on the outside of the HACS to increase the reflection of solar radiation on the surface of the TTI.

In the literature, there are few studies on the control of air-flow in passive systems. In the case of hybrid and HVAC systems, only electric damper actuators are used to control this air-flow [18]. In this work, two actuators were placed on both sides of HACS to open and close the lower and upper dampers, to allow the change between heating and cooling modes. Two electrical transformers (AT72D, AC) were used to supply them with electricity, controlled with an ON/OFF switch. Table A1 in Appendix B shows the relevant technical data. Two HACCP thermometers and two TMC20-HD temperature sensors were installed in the upper and lower sections of the HACS to measure the temperatures of the air that flows through the gap. Two 3667 temperature sensors were installed to measure the temperatures inside the adjacent box.

A 3447.38 kPa high-pressure gauge meter was connected to the TTI to record the gas pressure reached by the refrigerants when exposed to solar radiation. On the right side of the HACS, an opening was made to insert the PCM metal container. Inside this metal container, an analogue temperature data logger U12-012 was installed to record the temperature and relative humidity of the air inside the adjacent box. A 120V, 150W photocell, model FOBA-21, was used to turn the 9W LED bulb inside the box on and off during the winters of 2020 and 2021. These devices and the electric connection of the actuators are shown in Figure 3 [19,20].

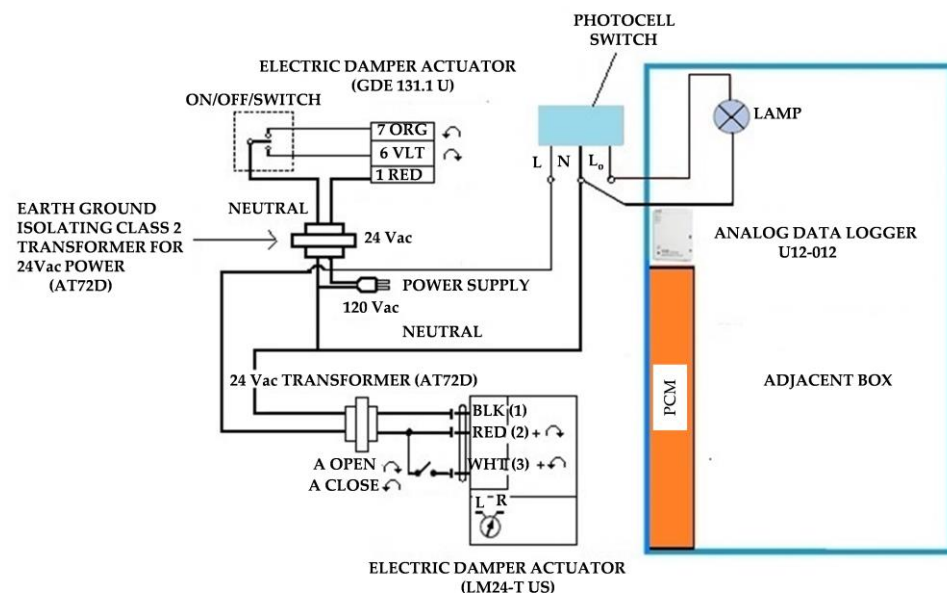


Figure 3. Electrical connection of damper actuators and lamp with photocell.

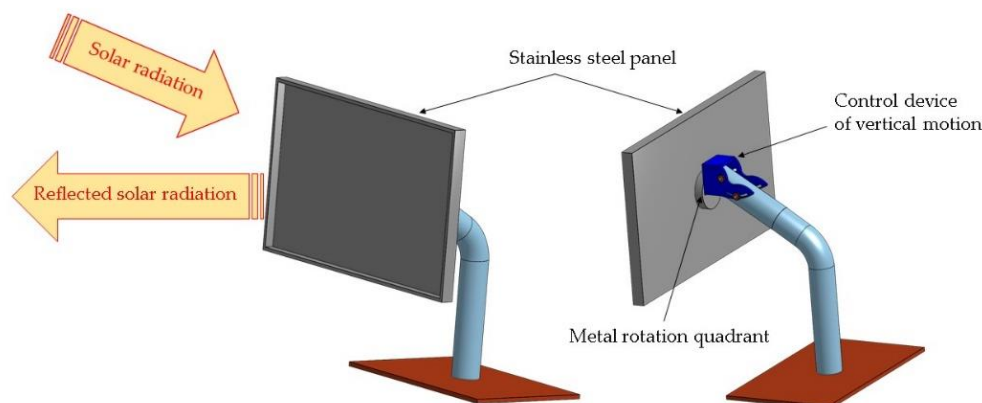
Materials such as pig fat have thermal inertia and can accumulate the solar radiation heat of the day and be used to heat the air inside the adjacent box at night. Pig fat changes from a solid to liquid state and is thus an attractive option as a PCM in the TTI. The data for the different physical parameters of pig fat from various sources were used. The general data on thermo-physical properties of pig fat and some organic PCMs are summarized in Table 1 [21–23].

Table 1. Thermo-physical properties of some organic PCMs and pig fat.

PCM	Units	Iraqi Paraffin	Paraffin Wax	Lauric Acid	Stearic Acid	Pig Fat
Melting temp.	°C	43	0–90	44	54	36–45
Liquid state density	kg/m ³	850	-	-	-	986
Solid state density	kg/m ³	950	880–950	66	940	910
Latent heat of fusion	kJ/kg	195	150–250	212	157	155–180
Thermal conditions	W/m °C	0.20	0.20	0.20	0.29	0.32–0.41
Liquid state specific heat	kJ/kg °C	2.10	-	-	-	2.05
Solid state specific heat	kJ/kg °C	2.20	-	-	-	2.03

A further advantage of this material is that it is easily obtainable from any butcher's shop, while more conventional PCMs must be imported, for example from the USA and Spain, therefore having important economic implications to a project.

The PCM metal container was made of gauge-22 galvanized-steel sheet and the edges were welded with an argon–oxygen blend and 50% lead–50% tin solder to prevent leakages of the liquid pig fat. The solar reflector panel was made of gauge-24 stainless steel. It had four L-shaped metal edges and was screwed to the metal base, as shown in Figure 4. The panel reflected solar radiation towards the front of the TTI from 6:00 a.m. to noon.

**Figure 4.** Sketch of the solar reflector panel.

Refrigerants R134a and R1233zd Used as Filler Gases in the TTI System

In Mexico, the most commonly used refrigerants for air conditioning and refrigeration are R22, R410A and R134a.

Refrigerants such as R11 and R12 may be thousands of times higher in GWP than carbon dioxide. Refrigerants such as R1233zd, R1234yf and R1234ze have the lowest GWP in comparison with modern refrigerants such as R134a and 410A [24,25]. Table A2 in Appendix C shows the GWP index and ASHRAE flammable classification of eleven common refrigerants. It is worth noting that in recent years, many international companies have developed new refrigerants to combat the depletion of the planet's ozone layer.

2.3. Removing Air and Moisture from the TTI

The TTI was charged with R134a on 28 July 2020, and with R1233zd on 7 April 2022, by injecting the refrigerant vapour inside the device. All TTI materials were designed to operate free of moisture and non-condensable gases, as the presence of moisture in the TTI can lead to rust formation. Air and moisture were thus removed to ensure this does not occur, as follows:

1. The yellow hose of the vacuum pump manifold was connected to the inlet coupling and the blue hose to the inlet of the TTI valve. The vacuum pump power switch

was turned on and the low-pressure valve was opened until the pressure gauge read 0.35 bar.

2. 10 min elapsed to hold the vacuum between 0 and 0.35 bar.
3. The vacuum pump was replaced by a gas cylinder and the low-pressure valve of the manifold was opened.
4. The refrigerant was charged until the low-pressure gauge read 0.35 bar and the mass of the refrigerant container weighed 25 g.
5. The low-pressure valve was closed, and thermal expansion was observed in the acrylic coating.

2.4. Measuring the Air Gap Temperature

Figure 5 shows a rectangular channel that is composed of the metal container of the TTI, two exterior walls of the HACS and one wall of the adjacent box. In this channel, the air chamber flows inside the adjacent box.

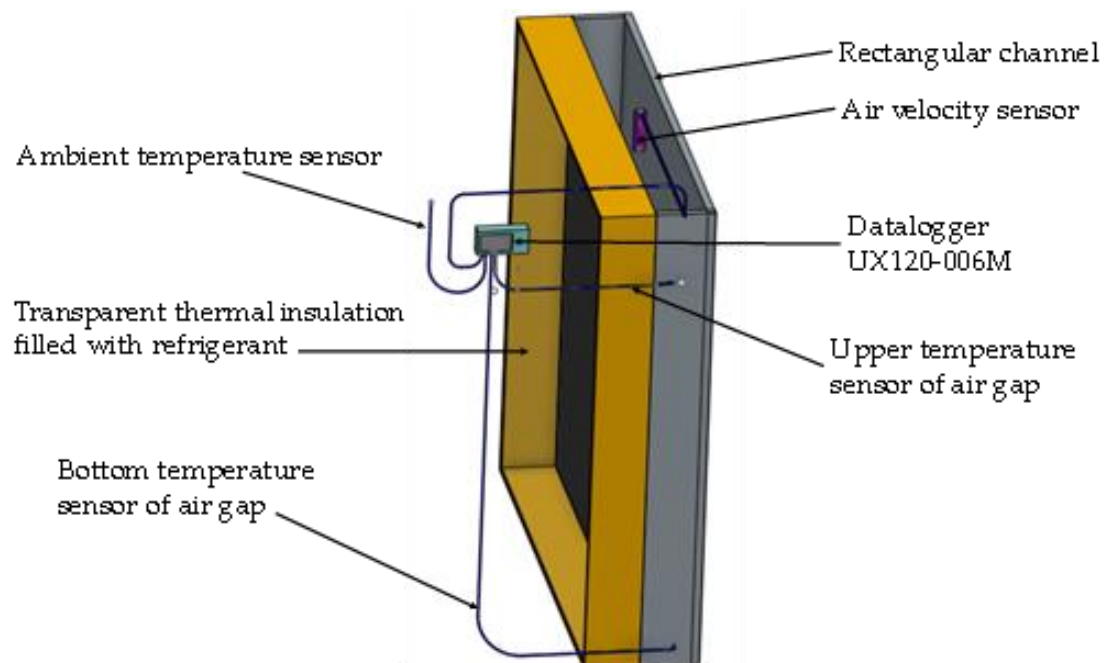


Figure 5. Arrangement of devices to record temperatures at the air gap.

The temperatures at the upper and lower parts of the air gap were recorded with the data logger UX120-006M, and the data logger 1400 recorded temperatures of the gypsum board and the air in the adjacent box. The air-flow between the black absorber and the gypsum board was heated to above ambient temperature by the HACS.

In 2020, the maximum temperature recorded in upper air gap was 48.90 °C. The following year, the maximum was 54.9 °C, while in 2022 it was 55.30 °C. These temperatures were plotted using the Grapher program 15 and are shown in Figure 6.

2.5. Measuring Temperature and Relative Humidity of the Air Inside the Box

The temperature and relative humidity of the air inside the box was recorded using the analogue data logger U12-012, from 6 to 16 August 2021. Measurements were also taken in a second period: 23 March to 5 April 2022. The temperatures are shown in Figure 7. The temperature and its relative humidity of the air inside the box are shown with the green and the navy blue lines, respectively.

In both figures, the green line shows that the air inside the box increased in temperature as time progressed in both 2021 and 2022. The analogue data logger recorded relative humidity values for the air inside the box air of less than 50% in March 2022.

Three temperature sensors were connected to the analogue data logger 1400 to record inside air temperatures of the adjacent box and the temperatures of the gypsum board between the air gap and PCM container from 8 May to 31 December 2021, and from 4 May to 28 June 2022. The gypsum board temperatures were always higher than the air temperatures because the board was heated by convection in the air gap. These recordings are shown in Figure 8.

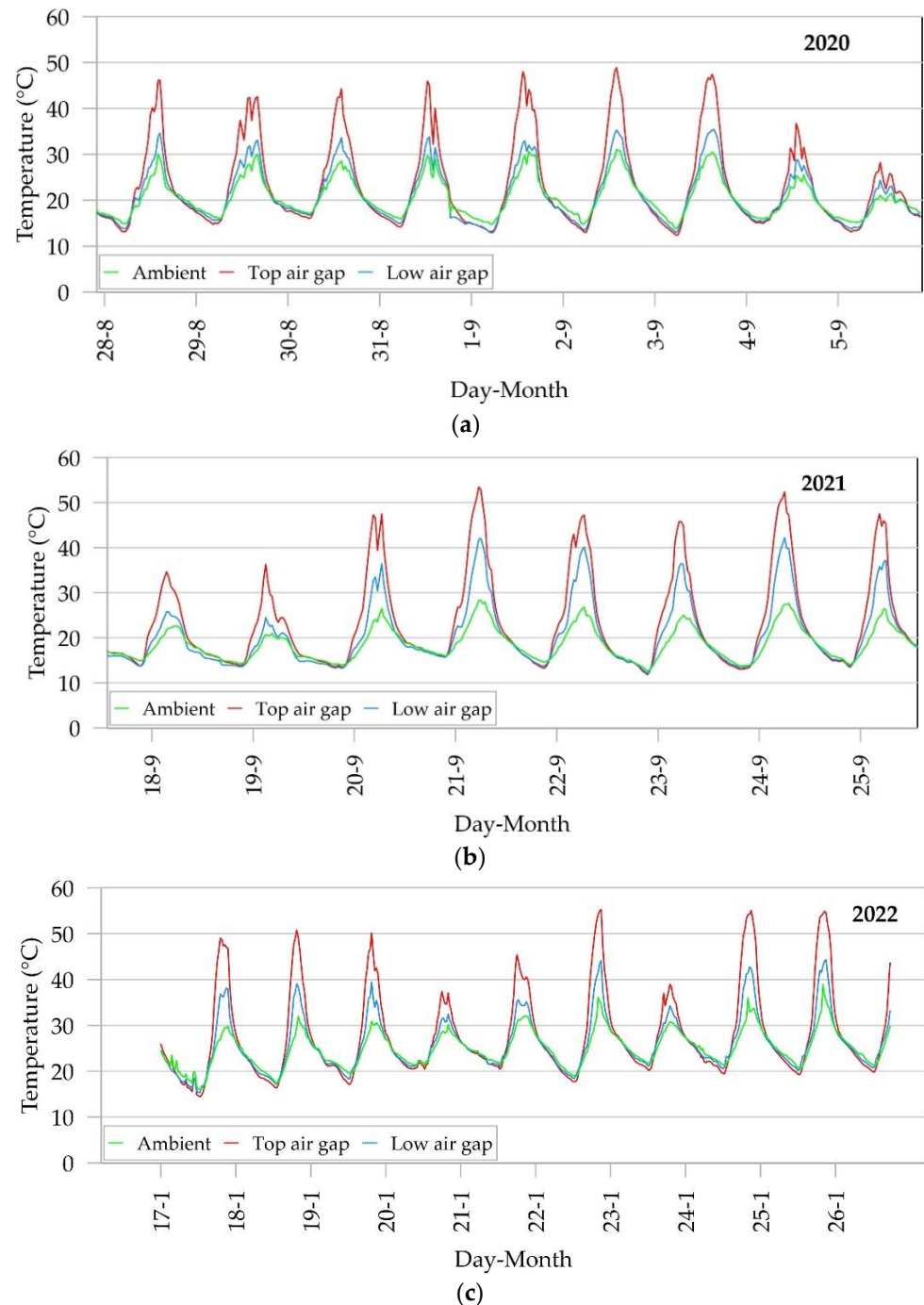


Figure 6. Temperatures recorded in (a) 2020, (b) 2021 and (c) 2022.

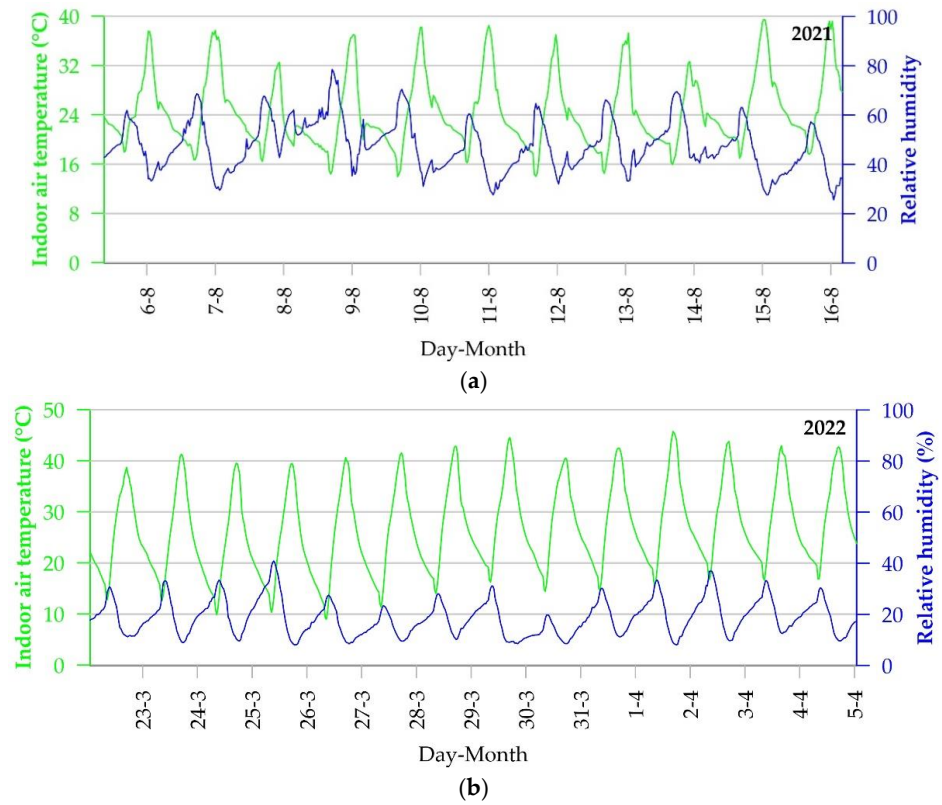


Figure 7. Temperature and relative humidity of the air inside the box for (a) 2021 and (b) 2022.

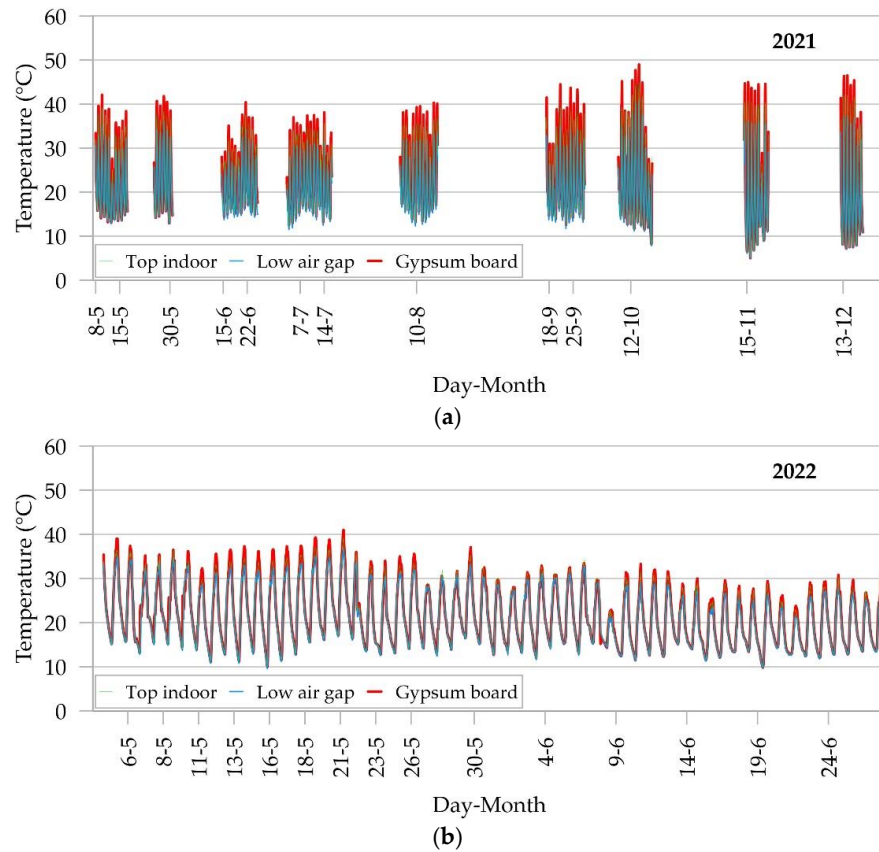


Figure 8. Temperatures of inside air and gypsum board: (a) 2021 and (b) 2022.

2.6. Recording Solar Radiation

The recordings of solar radiation in Netzahualcoyotl City and the inside air temperatures of the adjacent box, recorded in 2021 and 2022, are shown in Figure 9. The solar radiation of site is shown the red color and the temperature of the air inside of the adjacent box in the navy blue color. Although there was less solar radiation in November and December than in September and October, the blue line shows an average air temperature in the box of 35 °C when the upper damper was opened, Figure 9a, and an average air temperature in the box of 36 °C in April, May and June, when the upper damper was closed, Figure 9b.

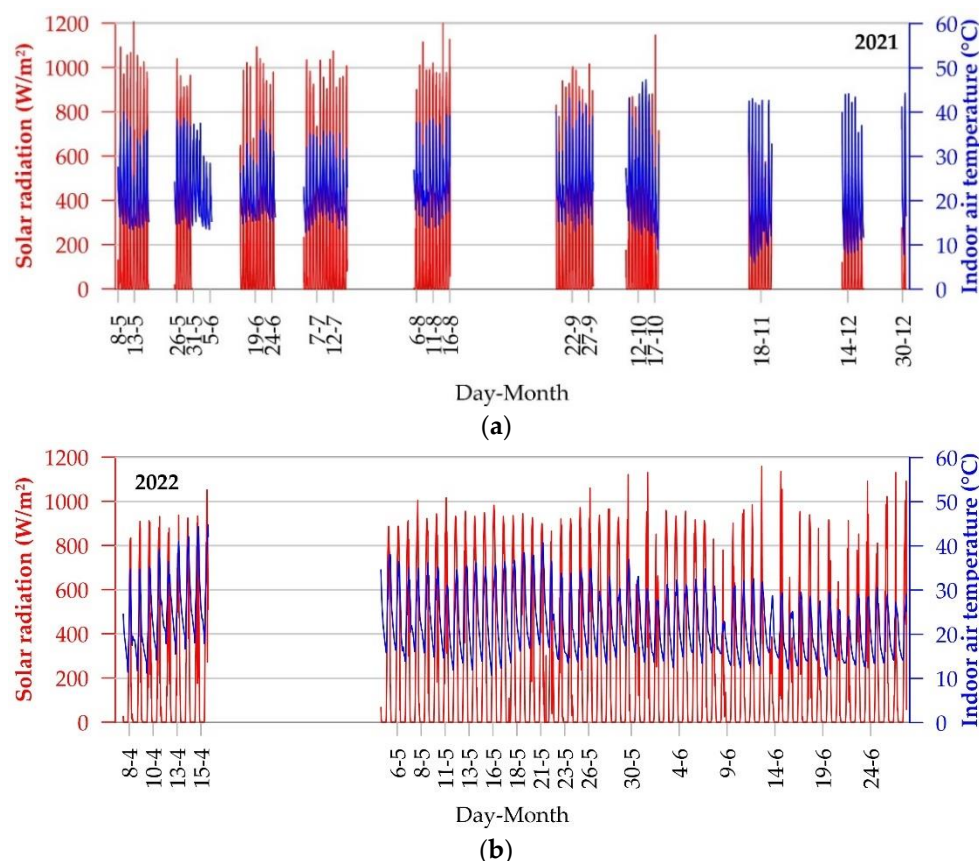


Figure 9. Solar radiation in Netzahualcoyotl and the air temperature in the box: (a) 2021 and (b) 2022.

2.7. Velocity of Air-Flow at the Air Gap

Sensor T-DCI-F-300-1A3, connected to data logger 1400, was used to measure the velocity of the air flowing between the bottom of the black absorber and the gypsum panel board every 30 min from 28 July 2020 to 25 September 2020, and then from 8 May 2021 to 29 May 2022. The maximum velocity was 1.49 m/s, at 12:00 a.m. on 6 August 2020. Figure 10 shows the maximum velocities at the air gap logged in 2020, 2021 and 2022.

2.8. Wind Velocity and Air-Flow in the Small Window

A small window, of 0.028 m², was opened on the exterior-right wall of the HACS to allow natural ventilation and avoid the build-up of pig fat odour. The renovation of the air inside was thus maintained when the upper damper was closed. An HER-440 digital anemometer, installed to measure the air-flow and wind velocity through the small window, recorded a maximum velocity of 1.98 m/s and maximum air-flow of 0.04 m³/s at 13:59 h on 22 July 2022.

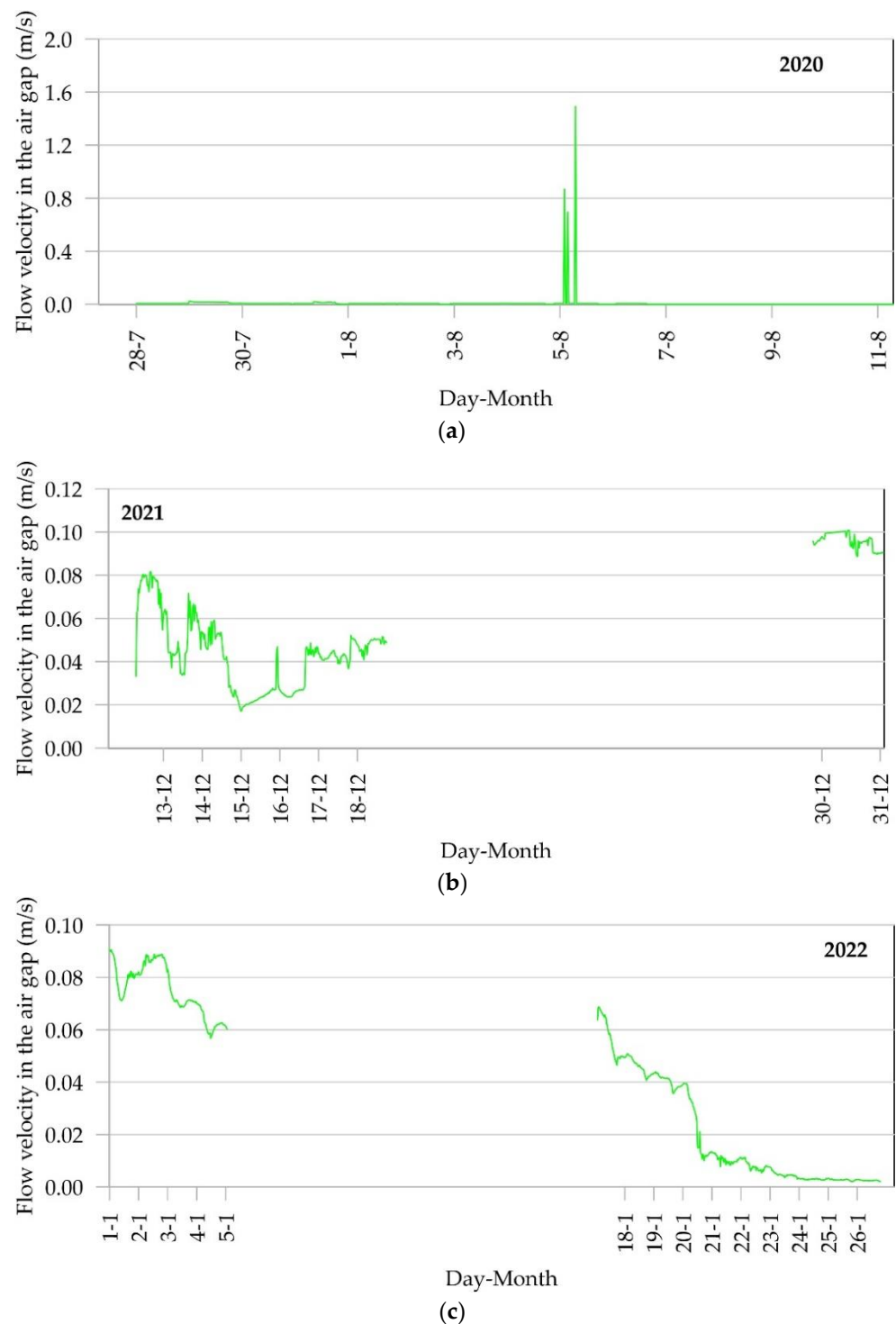


Figure 10. Velocity of air-flow at the gap: (a) 2020, (b) 2021 and (c) 2022.

2.9. Thermographic Monitoring

Infrared thermography (IRT) is often used to inspect buildings. The thermal images of the building elements, formed by the IR radiation emitted by them or reflected from their surface, means evaluation of the surface temperature distribution is possible and areas with humidity can be seen. IRT is mainly used for the detection of thermal bridges in walls, floors, roofs and windows, the detection of humidity zones in buildings walls, inspecting thermal insulation of walls and roofs, the study of thermal radiation and to identify heat loss in the refrigerant pipes of HVAC systems.

In this case, IRT was used to record the temperatures and make a quick diagnosis of the thermal performance of the TTI systems filled with R134a or R1233zd and the PCM, as well to explain their thermal behaviour during the day and at night.

The images of were captured with IR FlexCam thermal imager model Ti55FT-1111042, and the program used to analyse the images was SmartView 3.1.89.0. Figure 11 shows the maximum temperature of 46.17 °C (115.1 °F) during the day and 38.05 °C (100.5 °F) at night, in October. In both cases the upper damper was closed.

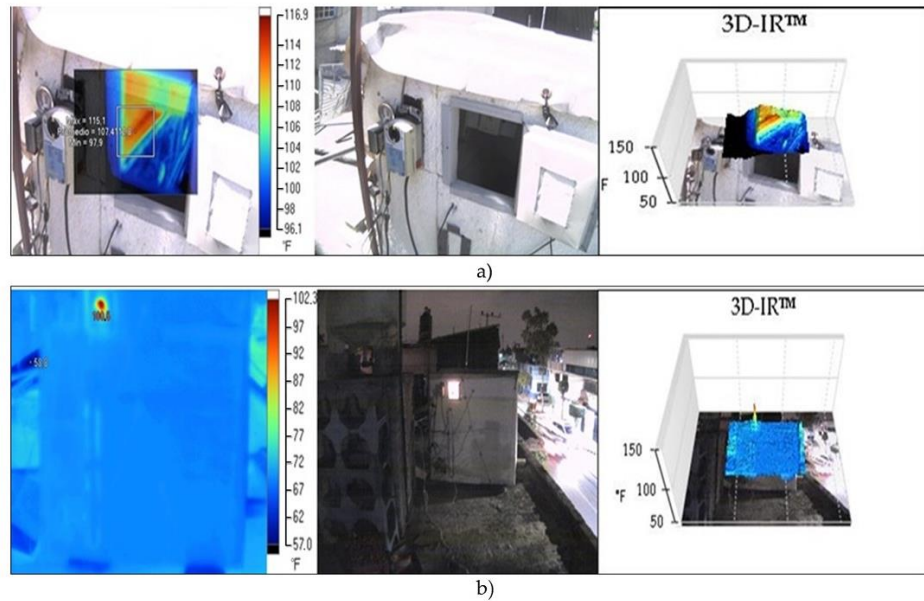


Figure 11. Thermal images of the HACS filled with R134a during the (a) day and (b) night.

Figure 12a shows a temperature of 22.50 °C (Sp1) during the night. Figure 12b shows temperatures of 36.80 °C (Sp5) and 40.1 °C (Sp4) on the diffusers. Two points on the metal absorber showed temperatures of 41.20 °C (Sp1) and 40.60 °C (Sp2), respectively. On one metal support 42.40 °C (Sp3) was recorded. The thermal images were taken with the upper damper closed, during the day.

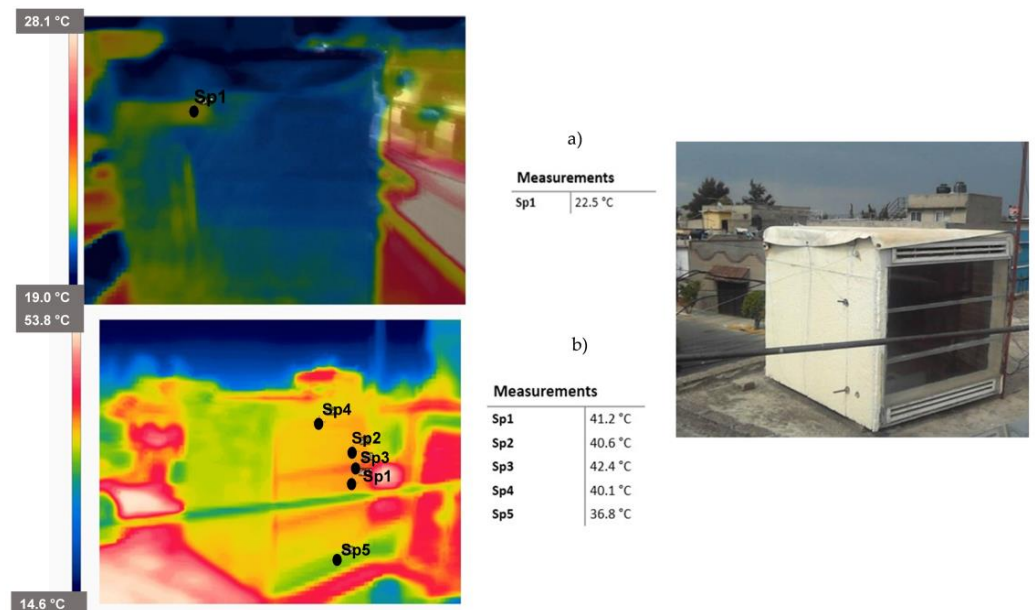


Figure 12. Thermal images of the HACS filled with R1233zd during the (a) night and (b) day.

Three computational 3D models of the TTI systems were made using the Opaque 3 Beta program to evaluate their thermal behaviour [26].

2.10. Design of Three TTI Models

The computational TTI models were built with their main front view facing south, and using data simulating the climate of Netzahualcoyotl, Mexico. The simulations were run to estimate heat loss, heat gain and reflected solar radiation of the three models. Table 2 summarizes materials used and their thermal resistance.

Table 2. Materials, total R-value and total U-value of the three TTI models.

TTI Filled with R134a	TTI Filled with R1233zd	TTI Filled with Krypton
Inside air film	Inside air film	Inside air film
Galvanized steel sheet	Galvanized steel sheet	Galvanized steel sheet
Pig fat	Pig fat	Micro-Phase Change Material 24D
Galvanized steel sheet	Galvanized steel sheet	Galvanized steel sheet
Plaster board	Plaster board	Plaster board
Air space (wall)	Air space (wall)	Air space (wall)
Steel sheet with black paint	Steel sheet with black paint	Steel sheet with black paint
Refrigerant 134a	Refrigerant 1233zd	Krypton gas
Acrylic sheet	Acrylic sheet	Acrylic sheet
Outside air film	Outside air film	Outside air film
Total R Value = 6.62 m ² -K/W	Total R Value = 8.67 m ² -K/W	Total R Value = 10.01 m ² -K/W
Total U-Value = 0.15 W/m ² -K	Total U-Value = 0.12 W/m ² -K	Total U-Value 0.10 W/m ² -K

MPCM 24D is a composite of micro-spheres filled with paraffin. The melting point of paraffin is 24 °C, the capsule composition is 85–90 weight percent PCM and 10–15 weight percent polymer shell. The mean particle size is 15–30 microns. Figure 13 illustrates the models of TTI systems.

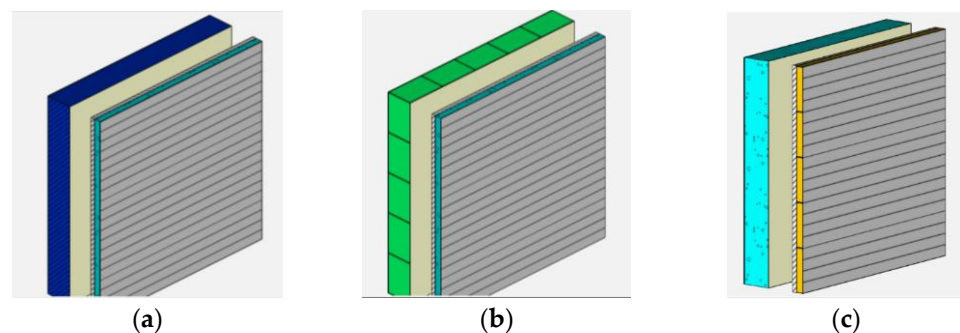


Figure 13. TTI models simulated with the Opaque 3 program and filled with (a) R134A–pig fat (b) R1233zd–pig fat and (c) krypton–MPCM 24D.

2.11. Comparison of Two TTI Systems

The study considered conditions of ambient temperature and the data logged at 23:00 h in August for the TTI filled with R134a and at 17:00 h in April for the TTI filled with R1233zd. Table 3 summarizes the boundary conditions for the heat-transfer analyses, with the upper damper closed.

Table 3. Boundary conditions of two TTI models filled with R134a and R1233zd.

Parameter	R134a	R1233zd	Unit
Ambient temperature	18.08	38.05	°C
Relative humidity	39.05	14.112	%
Solar radiation	0	630	W/m ²

Table 3. Cont.

Parameter	R134a	R1233zd	Unit
Exterior gypsum panel board temperature	23.10	44.90	°C
Interior surface temperature of metal refrigerant container	19.12	48.78	°C
Interior surface temperature in gypsum panel board	22.50	45.90	°C
Indoor air temperature	23.23	43.47	°C

Figure 14 shows a sketch of the design conditions to analyse the heat transfer of the TTI model filled with R134.

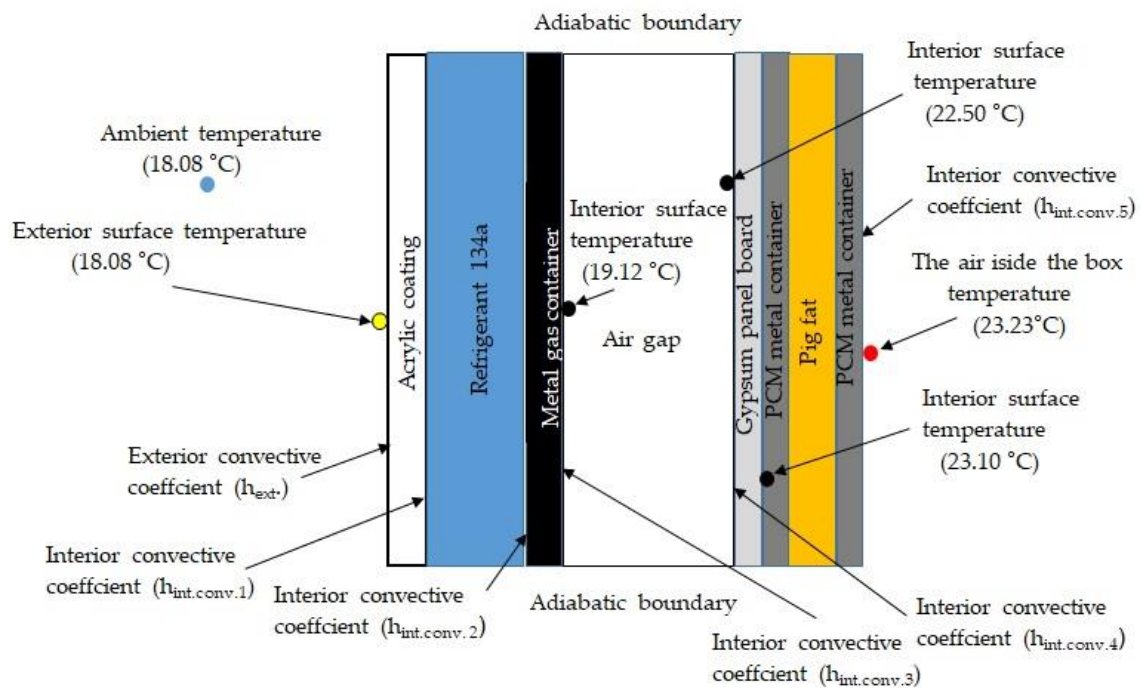


Figure 14. Boundary conditions of TTI filled with R134a and wall of organic PCM.

Churchill and Chu suggested a mathematical model to compute the Nusselt number with a constant surface heat flux and natural convection on the vertical plates [27]. The model is used to estimate the convective coefficients: $h_{ext.conv.}$, $h_{int.conv.1}$, $h_{int.conv.2}$, $h_{int.conv.3}$, $h_{int.conv.4}$ and $h_{int.conv.5}$.

The equation used to compute the heat flux is the following:

$$Q = U (T_{amb.} - T_{int.}), \quad (1)$$

where $T_{ext.}$ is 18.081 °C and $T_{int.}$ is 23.232 °C. U is the overall heat transfer coefficient, determined by the following equation:

$$U = \frac{1}{R_{Total}A} \quad (2)$$

where A is equal to 0.8534 m^2 and R_{Total} can be calculated as

$$R_{\text{Total}} = R_{\text{amb.}} + R_{\text{Acrylic}} + R_{\text{hint.conv.1}} + R_{\text{R134a}} + R_{\text{hint.conv.2}} + R_{\text{zinc galvanized sheet}} + R_{\text{Int.conv.3}} + R_{\text{Air}} + R_{\text{hint.conv.4}} + R_{\text{gypsum PB}} + R_{\text{zinc galvanized sheet}} + R_{\text{pig fat}} + R_{\text{zinc galvanized sheet}} \quad (3)$$

R_{Total} can also be computed as follows:

$$R_{\text{Total}} = \frac{1}{h_{\text{amb.}}A} + \frac{L_1}{k_{\text{Acrylic}}A} + \frac{1}{h_{\text{int.conv.1}}A} + \frac{L_2}{k_{\text{R134a}}A} + \frac{1}{h_{\text{int.conv.2}}} + \frac{L_3}{k_{\text{zinc galvanized sheet}}A} + \frac{1}{h_{\text{int.conv.3}}A} + \frac{L_4}{k_{\text{Air}}A} + \frac{1}{h_{\text{int.conv.4}}A} + \frac{L_5}{k_{\text{gypsum PB}}A} + \frac{L_6}{k_{\text{zinc galvanized sheet}}A} + \frac{L_7}{k_{\text{pig fat}}A} + \frac{L_8}{k_{\text{zinc galvanized sheet}}A} + \frac{1}{h_{\text{int.conv.5}}} \quad (4)$$

The thermal conductivity values for gypsum board and galvanized sheet metal ($0.43 \text{ W/m}^\circ\text{C}$ and $107.30 \text{ W/m}^\circ\text{C}$) were obtained from ASHRAE Fundamentals [28]. The thermal conductivity of $0.45 \text{ W/m}^\circ\text{C}$ for pig fat was taken from ASHRAE Refrigeration [29]. The thermal conductivity of 0.23 W/m K for acrylic was consulted in data sheets [30]. The thermal conductivity of R134a and R1233zd can be calculated with the refrigerant temperature and the Genetron Properties 1.4.1 program. The values of thermal conductivity, dynamic viscosity, specific heat and Prandtl number of air at different temperatures and pressure of one atmosphere were found in [31]. The R_{Total} was calculated as $12.20 \text{ m}^2\text{-}^\circ\text{C/W}$, yielding a U -value of $0.08 \text{ W/m}^2\text{-}^\circ\text{C}$ and heat flux of -0.36 W .

The process applied to calculate the heat flux of the TTI filled with R1233zd (second column of Table 2) and the R_{Total} was $12.12 \text{ m}^2\text{-}^\circ\text{C/W}$; the U -value was $0.08 \text{ W/m}^2\text{-}^\circ\text{C}$ and the heat flux was -0.38 W .

3. Results and Discussion

3.1. Results of Simulations with the Opaque 3 Program

The simulations run with the Opaque 3 program gave the heat gain–heat loss and reflected surface radiation of the three TTI models, seen in Figures 15 and 16, respectively.

Figure 15a shows a maximum heat gain of 1.51 W/m^2 and heat loss of -2.22 W/m^2 for the TTI model filled with R134a. Figure 15b shows a maximum heat gain of 0.96 W/m^2 and heat loss of -1.46 W/m^2 for the TTI model filled with R1233zd. Figure 15c shows a maximum heat gain of 0.10 W and heat loss of -0.60 for the TTI model filled with krypton.

At midday, in April, May, June, July and August, respectively, the reflected surface radiation computed with the Opaque 3 program was 110 W/m^2 , 115 W/m^2 , 0 W/m^2 , 110 W/m^2 and 105 W/m^2 . Figure 16 shows the reflected solar radiation over the faces of TTI models filled with R134a, 1233zd and krypton.

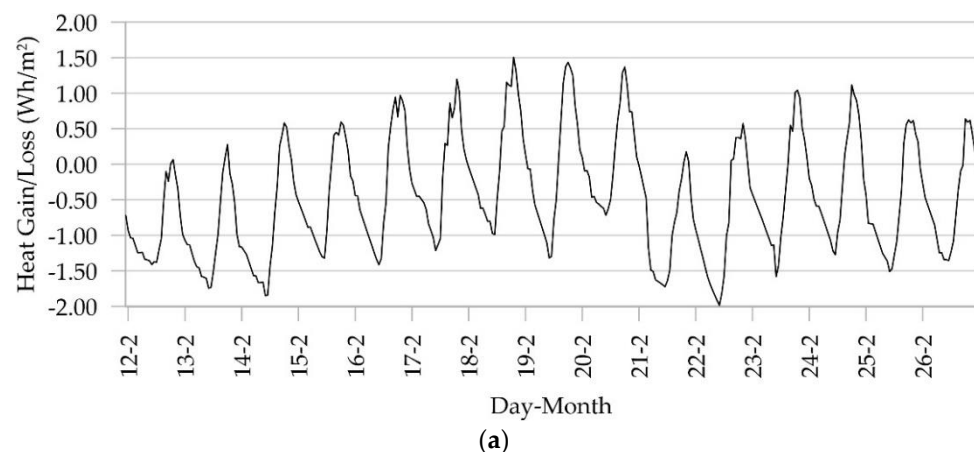
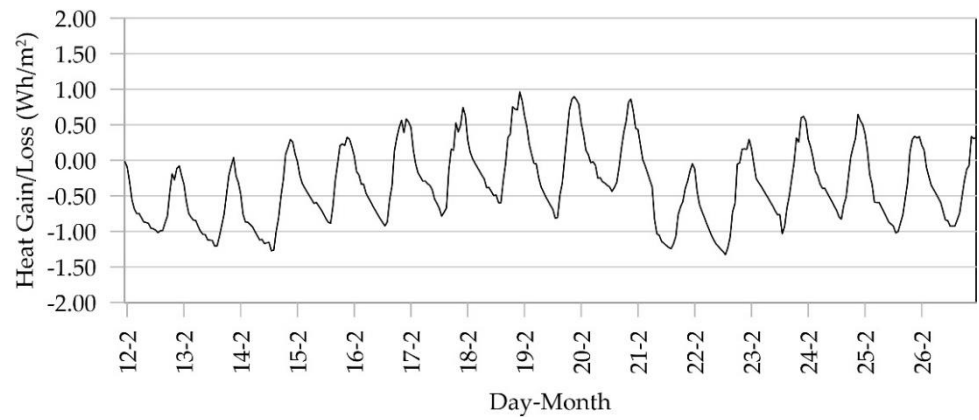
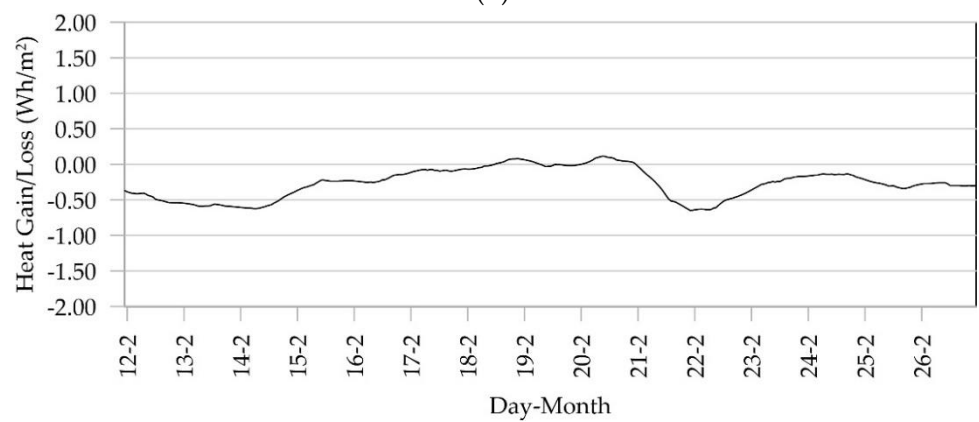


Figure 15. Cont.

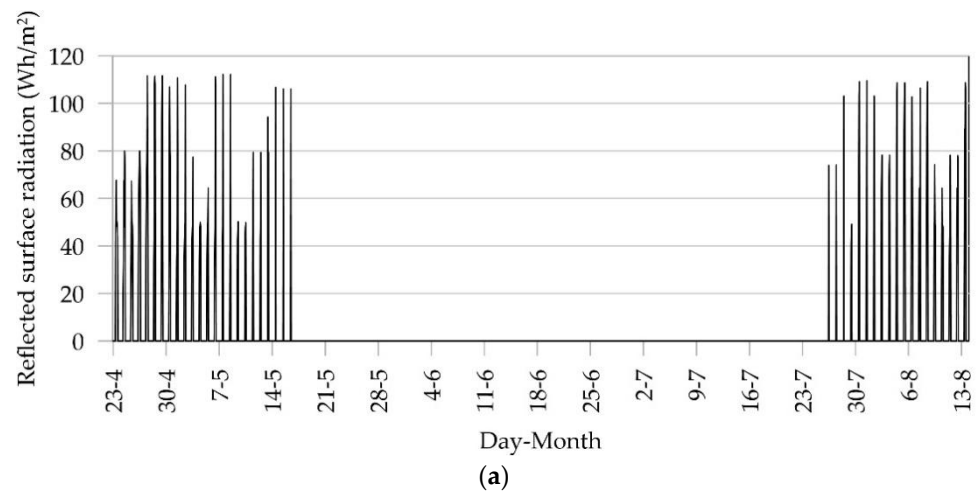


(b)



(c)

Figure 15. Heat gain and heat loss of the simulations of the Opaque 3 program and combinations of (a) R134a–pig fat, (b) R1233zd–pig fat and (c) krypton–MPCM 24D.



(a)

Figure 16. Cont.

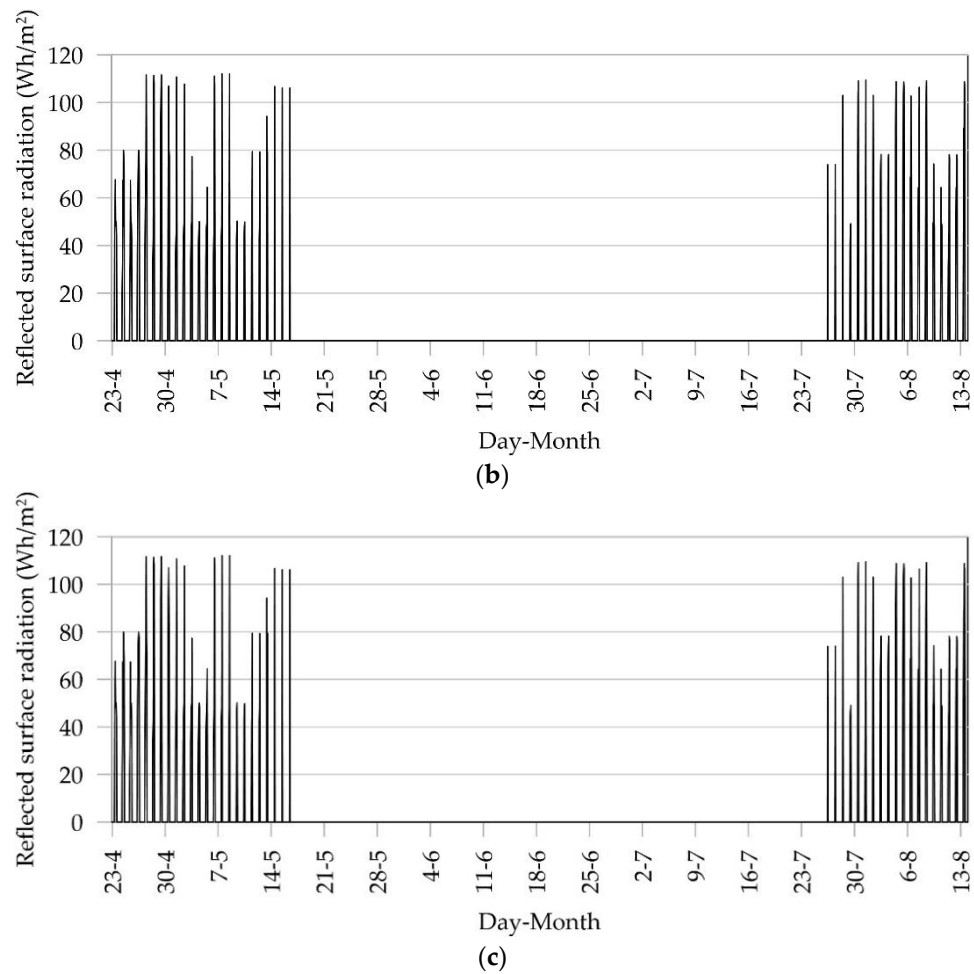


Figure 16. Reflected solar radiation over TTI systems simulated with the Opaque 3 program and filled with (a) R134a and pig fat, (b) R1233zd and pig fat and (c) krypton and MPCM 24D.

3.2. Comparison of Simulations and Measured Data

The SM206 solar power meter, used to measure the reflected surface radiations over the front face of the TTI filled with R1233zd, has a range of 0.10–1999.99 W/m² and wavelength 340–1100 nm. The measurements showed that part of this thermal energy was always reflected back to the surroundings. Figure 17 shows the reflected solar radiation at midday in April, May, June, July and August, 2022.



Figure 17. Reflected surface radiation of TTI filled with R1233zd.

A detailed comparison of the results computed with the Opaque 3 program and the data recorded with the solar power meter SM206 showed reflected solar radiation data differences of 26.70 W/m² in April, 83.20 W/m² in May, 49.80 W/m² in June, 87.90 W/m² in July and 21.98 W/m² in August.

3.3. CFD Simulations

After modelling the HACS with the ONSHAPE online platform, it was exported to the engineering software in the Cloud SIMSCALE to run scenarios of flow of the air gap, air-flow inside the adjacent box, and convection and conduction processes on the acrylic coating, the metal container and the black metal absorber of TTI filled with R134a and PCM [32,33].

3.3.1. Simulations of Air Velocity

The measured data from the analogue data logger UX-120-006, air velocity sensor T-DCI-F300-1A3 and temperature sensor TMC-20-HD in March were input into the SIMSCALE to run simulations of velocity and temperature of the air gap. The data of platform were velocity inlet of 0.5 m/s and velocity outlet of 0.00916 m/s at temperature of 24 °C. Simulation analysis was compressible type with k-omega SST turbulence model and transient time dependency. ParaView program was used to show the changes of temperature of the air gap inside the channel [34].

Moreover, the data logged with air velocity sensor T-DCI-F300-1A3 and the analogue data logger UX120-006M were input in SimScale tool to simulate the air velocity inside the adjacent box.

3.3.2. Simulations of Heat Transfer of TTI

Heat Transfer Simulations of the Black Metal Absorber

To study the thermal behaviour of the TTI in depth, a dynamic simulation of convective and conduction heat transfer of the container filled with refrigerant 134a and the steel absorber was performed using the SimScale tool at 16:00 h for the month of December.

The absorber is at the base of metal container. A temperature of 78.60 °C was found on various parts of the surface of the absorber. The maximum heat flux velocity on the surface was 2.03 m/s, with a maximum net radiative heat flux of 171.2 W/m² and a non-hydrostatic pressure of 101,325 Pa.

Heat-Transfer Simulations of the PCM

Two simulations of heat transfer by convection and conduction of the metal container filled with pig fat were run with laminar and k-omega SST turbulence models at 16:30 h for the month of December.

The results show, in the centre of the metal container, temperatures of 47.80 °C in the laminar model and 50.50 °C in the k-omega turbulence model. Both simulations gave a maximum temperature of 50.50 °C on the top area of 0.32 m² of the PCM metal container. All the simulation results are shown in Appendix D. Moreover, this simulation shows that incoming heat was absorbed via PCM during the daytime, and rejected into the interior air of the adjacent box during the night.

Comparative Analysis between Experimental and Simulated IAT

The IAT was estimated with spread sheet calculations of thermal mass, according to EN ISO 13,786 [35]. Mean side 1 temperature (T₁) and mean side 2 temperature (T₂) correspond to the ambient and the gypsum board temperatures, respectively. The spread sheet also computed a Total U-value of 0.14 W/m² K for the TTI system of R134a and pig fat with a thickness of 0.16 m. This Total U-value is similar to the 0.15 W/m² K shown in Table 2. Figure 18 shows the thermal behaviour of the experimental and estimated temperatures of the air inside the box from 8 to 17 May 2021.

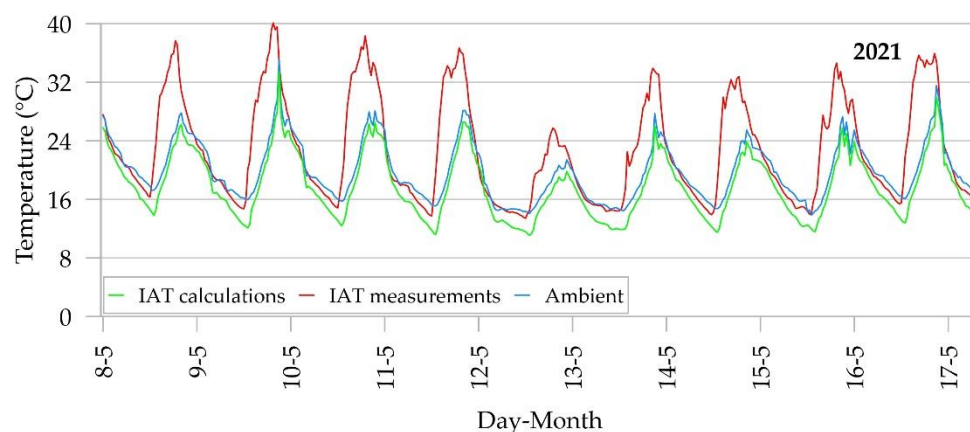


Figure 18. Experimental and estimated temperatures of the air inside the box 2021.

In this figure, the experimental air temperature in the box is higher than the estimated value because pig fat accumulates heat during the day and loses it to the air inside the adjacent box at night. The estimated air temperature inside the box (red line) shows similar thermal behaviour to the ambient temperature (blue line) and the experimental temperatures of the air inside the box (green line) in part of the nights.

3.4. Comparative Analysis

3.4.1. Analysis of the Results of the Simulations and the Heat Transfer of the TTI Systems

In the case of the R134a TTI, there is a difference of 1.87 W between the results of the Opaque 3 program and the heat-transfer analysis, 1.51 W and -0.36 W, respectively. In the case of the R1233zd TTI, with results of 0.96 W and -0.38 W, there is a difference of 1.34 W.

3.4.2. The Thermal Behaviour Analysis of the HACs

Table A1 in Appendix B shows that the damper actuators LM24-T US must be in ambient temperatures of below 54.44 °C, while Figure 6c shows that the top air gap has temperatures of over 50 °C. These damper actuators should not be used in an HACs as the hot air can burn the copper wire coils.

Figure 9a shows the air temperatures in the adjacent box are over 40 °C with average solar radiation of 800 W/m² in November and December. The same figure shows that the HACs can heat up the air in the box for several hours during the night.

Figure 10a shows a maximum air gap velocity of 1.49 m/s that indicated constant movement of the air gap inside the HACs in the heating mode. Factors such as the design of the linear diffuser and the wind direction probably influenced the flow velocity at the air gap.

In the case of the thermal images, Figure 11 shows that the HACs had a maximum daytime temperature of 46.17 °C, and 38.05 °C at night. The Opaque program computed a heat gain of 0.96 W in the TTI filled with refrigerant 134a and pig-fat-based PCM. This heat gain is greater than the 0.10 W computed in the TTI filled with krypton and MPCM 24D.

Figures 7, 9, 11 and 12 illustrate the heat storage property of pig fat and reach a maximum temperature of 50.50 °C in the upper 0.20 m² of the metal container of the PCM.

All simulations were run with online platforms and free software and used some data from temperature and air velocity records, solar radiation and solar power meter measurements. To better illustrate the thermal and dynamic behaviour of the system, the results show some HACs devices, such as the metallic PCM container, the black steel absorber and gases in the air gap of the adjacent box and R134a in TTI. Figure A6 in Appendix D shows the temperatures of 18.08 °C in the centre of the R134a filled TTI. A simulation of the heat transfer analysis was run in order to model the effects of turbulence.

3.4.3. Convergence Criterion for CFD Simulations

In the figures, the SIMSCALE online platform shows residuals that represent the solution imbalances in its CFD simulations. These residuals should be as small as possible, below 0.001, and are marked in the graphs with the letter e. These values also describe the stability of a solution, however the curves with sudden spikes show that results of such simulations are not reliable. According to SIMSCALE, each convergence point represents the average of each variable for every iteration, normalized to a range of 0–1. In the simulation, the calculations began with the initial estimations of velocity and the temperatures at the air gap, of the air inside the adjacent box and of the heat flux of the metal PCM container and the black steel absorber. At each iteration, the calculated values are updated with respect to the results of the previous iteration. In the converged steady-state solution, the calculated values no longer change.

At the air gap, the convergence plot started at 6.76×10^{-5} s, with an e-value of 0.009869056. The numerical simulation in steady state of the air inside the adjacent box shows a convergence plot at 920 s, with velocities of $U_x = 0.039849115$ m/s, $U_y = 0.012201261$ m/s, $U_z = 0.014132835$ m/s and an e-value of 0.00998446. In the k-epsilon turbulence model and transient state the iterations were increased from 652 to 1,000, and the simulation time from 2 s to 3 s, because the minimum e-value was 0.005791949. Regarding the black absorber of the R134a TTI, the residual values showed no oscillations at 80 s when the heat flux velocities were $U_x = 6.57 \times 10^{-5}$ m/s, $U_y = 5.29 \times 10^{-5}$ m/s and $U_z = 3.30 \times 10^{-6}$ m/s. The simulation curves for the PCM metal container with laminar and k-omega SST turbulence models were stable at 1600 s and 2000 s, with e-values of 0.01 and 0.000001, respectively.

The simulation of heat transfer by convection of the R134a TTI with the k-omega SST turbulence model was stable at 1800 s with an e-value of 1×10^{-8} .

4. Conclusions

HVAC systems are composed of many mechanical, electric and electronic devices that depend on increasingly complex control systems, such as BMS and Artificial Intelligence. Such complicated control systems are always connected to electricity and internet, and are, therefore, expensive in terms of maintenance and energy consumption; when failure occurs, they require specialist technicians. The HACs described in this paper has no sophisticated temperature and humidity controls and is therefore an attractive option as a low-tech system for supervisory control and data acquisition in the heating and cooling of buildings. The main findings of this study can be summarised as follows:

- Currently, refrigerants are used in the mechanical circuits of refrigeration and air-conditioning systems, but have not been used in TTI applications. Refrigerants are sought for these systems with low thermal conductivity and low global warming potential. Under real conditions, in Nezahualcoyotl City, these transparent thermal materials have similar thermal behaviour to noble gases, and TTI filled with a combination of R134A or R1233zd and pig fat were found to be non-flammable.
- Safe gases that do not destroy the ozone layer can be a viable, sustainable option for heating buildings with a solar radiation of over 800 W/m^2 .
- The TTI of an HACs can be charged with different refrigerants that are not dependent on the use of a noble gas such as krypton. In these experiments, pig fat was shown to be a non-flammable organic material that could be used in the passive system of a building.
- Overheating in the air gap can be controlled using Ni-Ti actuators, as these materials change their physical dimensions at $23 \text{ }^\circ\text{C}$ cooling temperature and $70 \text{ }^\circ\text{C}$ heating temperature. The Ni-Ti actuators will open the dampers at $23 \text{ }^\circ\text{C}$ and close them completely at $51 \text{ }^\circ\text{C}$ in the cooling mode.
- The air gap can increase the airflow velocity from the adjacent box by means of a fan, which could be powered with a 5 W solar panel plate and installed on the roof of the HACs.

- The use of phase-change interior thermal materials will be more common in passive heating systems of buildings.
- In this study digital twin solutions that combine data streams from individual devices and implement new simulations, and that can optimise their performance and thus decrease their impact on the environment, were sought for bioclimatic architecture by means of an HACS.
- In the future, CFD simulations should be run with measured data, transient heat-transfer and turbulence models to improve the accuracy of the simulation results and the thermal behaviour of HACS in different meteorological conditions, and to improve HACS design.

Author Contributions: Conceptualization, A.T.R. and D.M.G.; methodology, A.T.R. and R.S.C.; software, A.T.R.; validation, A.T.R. and R.S.C.; formal analysis, A.T.R.; investigation, A.T.R.; resources, A.T.R.; data curation, A.T.R. and D.M.G.; writing—original draft preparation, A.T.R., I.G.K. and R.S.C.; writing—review and editing, R.S.C.; visualization, A.T.R.; supervision, R.S.C.; project administration, A.T.R. and D.M.G.; funding acquisition, A.T.R. and D.M.G. All authors have read and agreed to the published version of the manuscript.

Funding: This research was funded by the Mexican Centre for Ocean Energy Innovation (CEMIE-Océano, Centro Mexicano de Innovación en Energía del Océano) CONACYT-SENER Sustentabilidad Energética project: FSE-2014-06-249795.

Data Availability Statement: Data available on request due to restrictions of privacy. The data presented in this study are available on request from the corresponding author. The data are not publicly available due to their continue update.

Acknowledgments: The authors acknowledge the support of the Engineering Institute, UNAM for supplying an IR FlexCam thermal imager model Ti55FT-1111042 and SmartView 3.1.89.0 program. The authors are also grateful to Sebastian Block, support engineer of SimScale GmbH, Munich, Germany, for the facilities granted for use of the simulation software SimScale.

Conflicts of Interest: The authors declare no conflict of interest.

Appendix A. Building the HACS

The main steps in building the HACS are shown in Figure A1, including the devices and construction materials used.

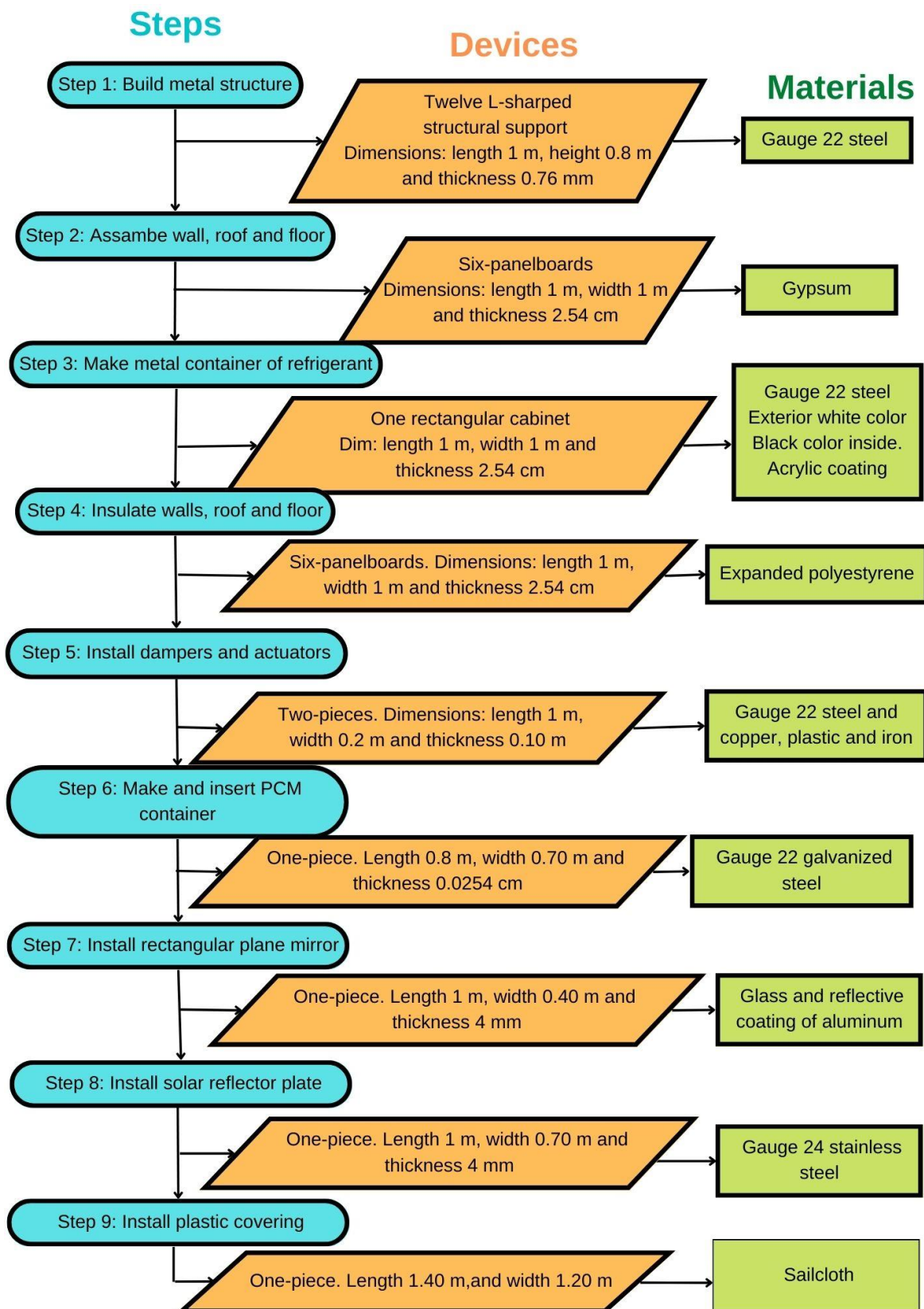


Figure A1. Steps in building the HACS.

Appendix B. Technical Data of Actuators

Table A1. Technical specifications of the actuators.

	Bottom Actuator	Top Actuator
Model	LM24-T US	GDE 131.1U
Power supply	24 VAC \pm 20% 50/60 Hz 24 VDC \pm 10%	24 Vac +20%, -15%, 50/60 Hz
Power consumption	2 W	
Transformer	3 VA (Class 2 power source)	2.3 VA
Electrical connection	3 ft, 18 GA, UL CL2P plenum cable	3 ft, 18 GA, UL CL2P plenum cable
Control	On-Off	On-Off
Overload protection	Electronic throughout 0 to 95° rotation	Electronic throughout 0 to 95° rotation
Angle of rotation	Max. 95°, adjust. with mechanical stops	0° to 90° with 5° intervals
Torque	Min 4 N-m	5 N-m
Direction of rotation	Reverse wires terminals 2 and 3	Reverse wires terminals Y1 and Y2
Running time	80 to 110 s for 0 to 35 in-lb	90 s at 60 Hz (108 s at 50 Hz)
Manual override	External push button	External push button
Humidity	5 to 95% RH, non-condensing	95% RH
Ambient temperature	-30 °C to 50 °C	-32 °C to 54.44 °C
Storage temperature	-40 °C to 80 °C	-40 °C to 70 °C
Housing type	NEMA type 2 (-T models NEMA 1)	Class 2 according to UL, CSA
Electrical connection	Screw terminal (for 26 to 14 GA wire)	Class III per EN60730
Housing material rating	UL94-5V	Screw terminal (18 GA wire)
Noise level	Less than 35 dB (A)	NEMA Type 2 IP54 according to EN 60 529
Servicing	Maintenance free	-
Quality standard	ISO 9001	Maintenance free
Weight	0.55 kg	0.48 kg

Source: Envirotrolsgroup and Siemens industry.

Appendix C. GWP Index and Physical Properties of Commonly Used Refrigerants

Table A2 frames the relative GWP index and ASHRAE flammable classification of common refrigerants. The higher the GWP value, the more potential to warm the Earth, compared to carbon dioxide (which is the baseline listed, with a GWP of 1).

Table A2. GWP index and physical properties of commonly used refrigerants.

Refrigerant	GWP Index	Liq. Temp. (°C)	Liq. Pressure (kPa)	Liq. Therm. Conductivity (mW/m-K)	Vapor Therm. Conductivity (mW/m-K)	ASHRAE Flammable Classification
R1233zd	5	46.85	266.80	72.10	12.22	A1
R1234yf	0	46.85	1207.20	62.94	16.44	A2L
R1234ze	1	46.85	919.60	71.69	15.66	A2L
R11	4660	46.85	215.10	80.67	9.42	A1
R134a	1300	46.85	1216.60	71.78	16.30	A1
R12	10,200	46.85	1130.50	59.64	11.94	A1
R123	79	46.85	192.60	70.59	10.50	B1
R141b	782	46.85	165.80	80.63	11.46	A1
R22	1760	46.85	1806.10	73.40	13.77	A1
R410A	1130	46.85	1362.20	72.64	14.36	A1
CO ₂	1	28.85	7062.80	84.45	71.01	A1

Source: Honeywell and ANSI/ASHRAE Standard 34-2019.

Appendix D. Simulations

Figure A2 shows an approximate air velocity of 1.10 m/s and temperature of 24.10 °C (297.25 K).

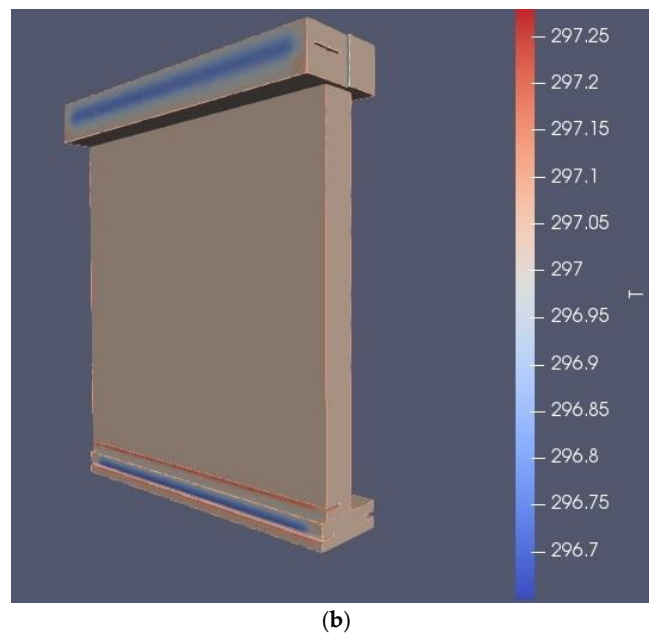
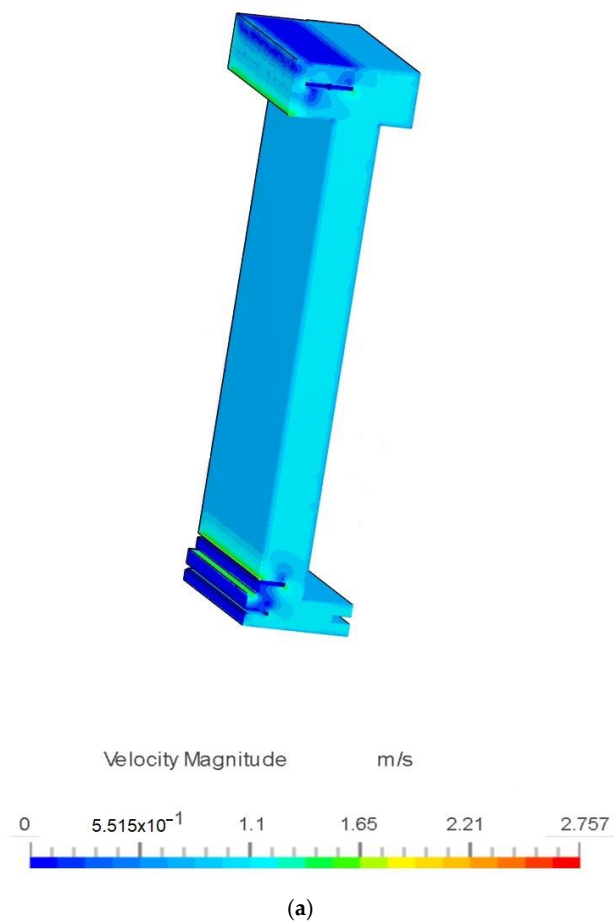


Figure A2. CFD simulations of (a) velocity and (b) temperature of the air gap.

Figure A3a shows the inlet velocity and the outlet velocity of 0.08173 m/s with the laminar and steady state model. In this case, the velocity of the air inside the box was constant because it did not change with the time. A new simulation was performed with the same software for the same month with the k-epsilon turbulence model in transient state to compare the two types of airflow motions. Figure A3b shows the air simulation with the k-epsilon turbulence model.

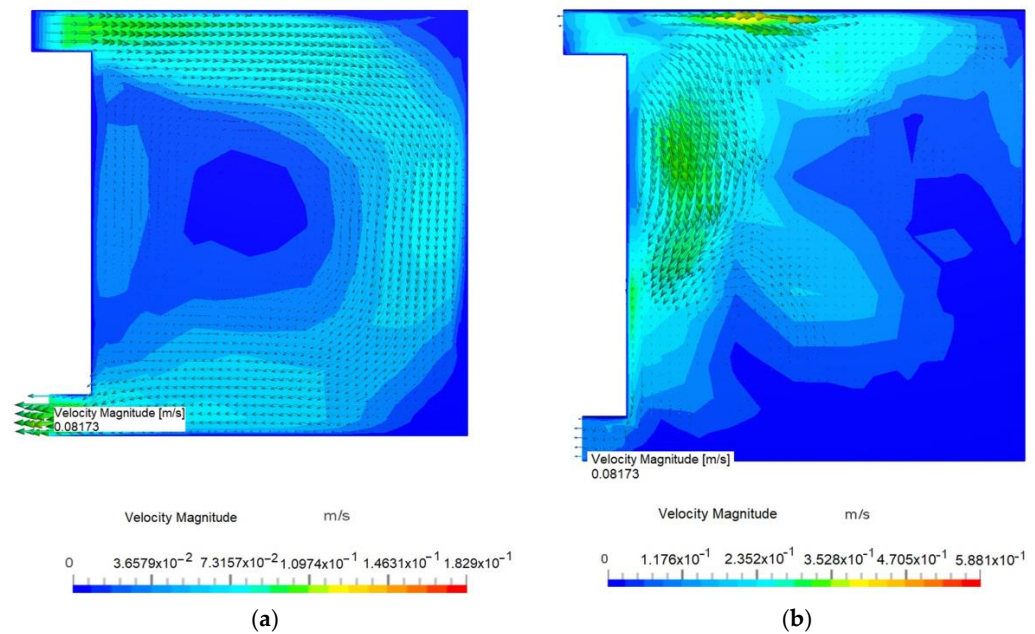


Figure A3. Movement of air inside the adjacent box with the laminar model and (b) with the k-epsilon turbulence model. (a) In this case, the velocity of the air inside the box was constant because it did not change with the time.

Figure A4 shows temperature, heat flux and net radiative heat flux on the black absorber of the TTI filled with R134a. The dots show a minimum of 0 m/s, average of 4.964×10^{-1} m/s and maximum velocity of 2.03 m/s over surface area of the black absorber. An integral value of the heat flux and volumetric flow rate over the same surface are shown of 2.259×10^{-1} m³/s and 1.35×10^{-2} m³/s, respectively. In the case of net radiative heat flux, the same parameters were simulated and presented in Figure A4b).

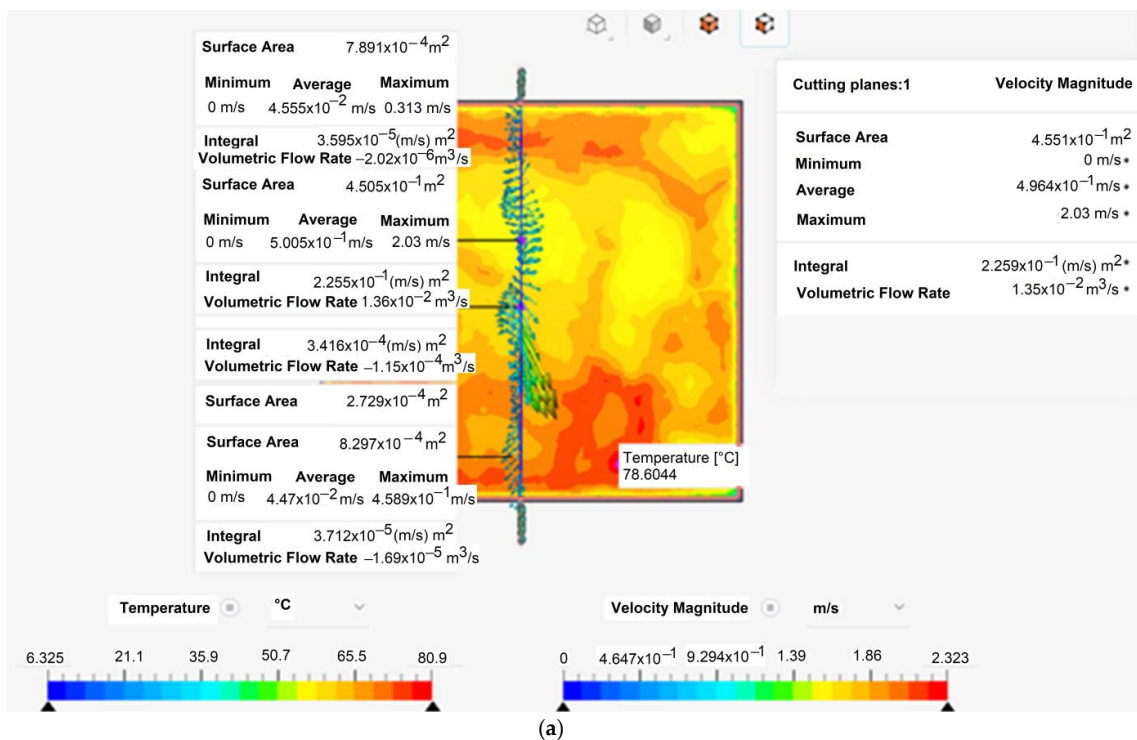


Figure A4. Cont.

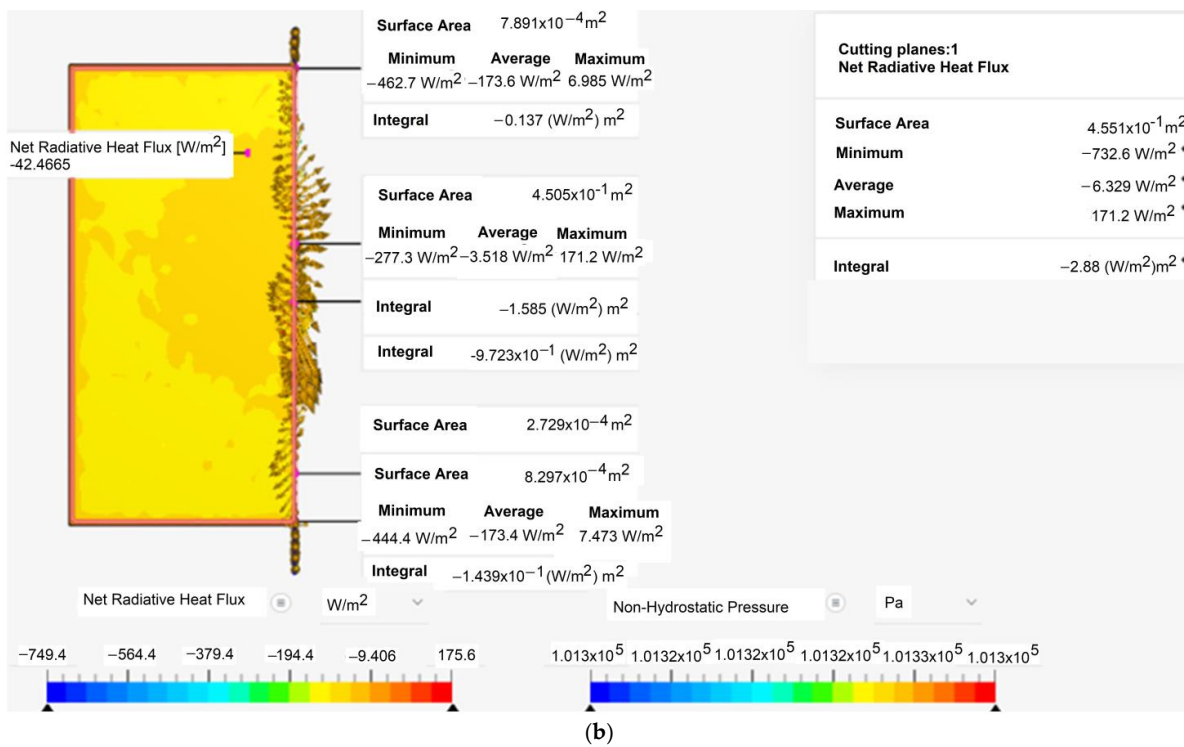


Figure A4. (a) Temperature, maximum heat flux velocity and (b) maximum net radiative heat flux on the black steel absorber.

Figure A5 shows the thermal behaviour of the PCM with the laminar model and the k-omega STT turbulence model.

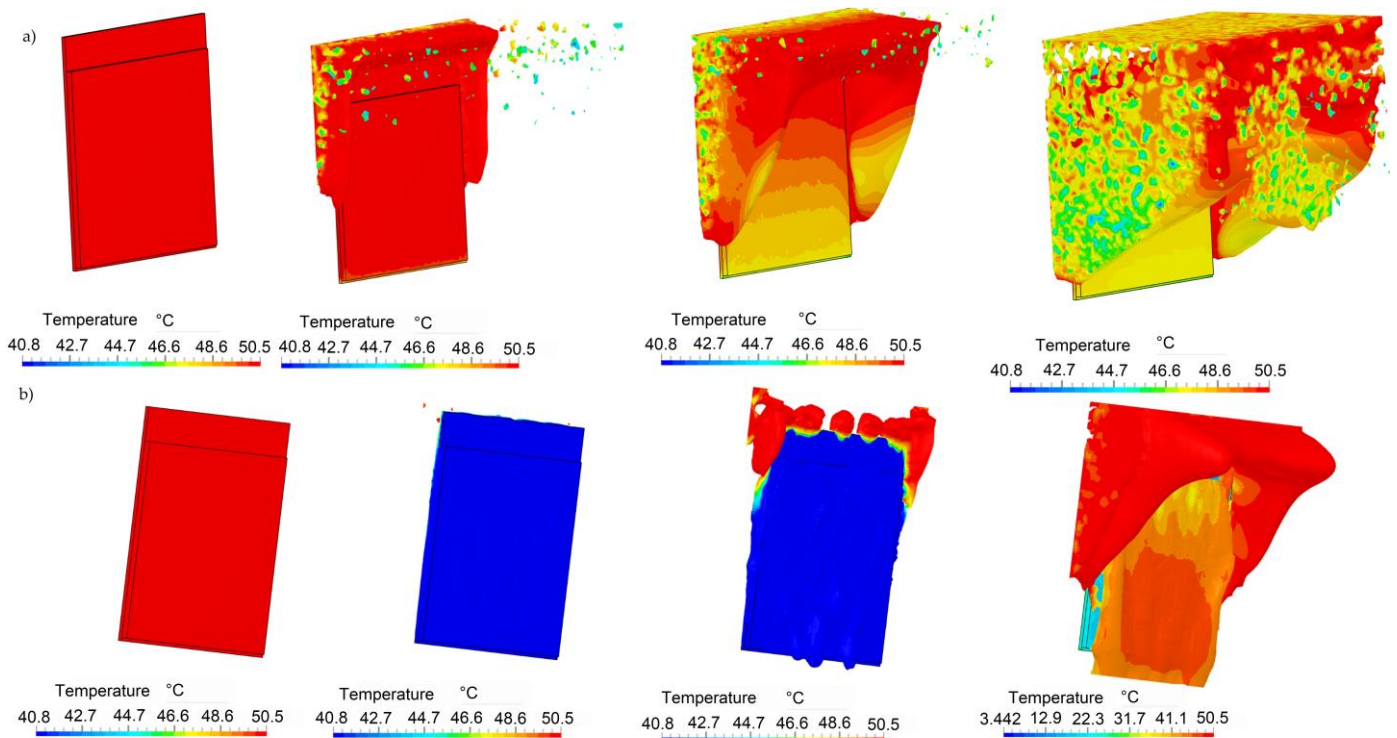


Figure A5. Simulations of the PCM metal container with (a) laminar model and (b) k-omega STT turbulence model.

A simulation of the heat transfer by convection of the R134a filled TTI was run with the k-omega SST turbulence model at 11:00 h in August, 2021. The results, seen in Figure A6, show a temperature in the centre of 18.08 °C, and 18.60 °C around the four edges of the TTI model.

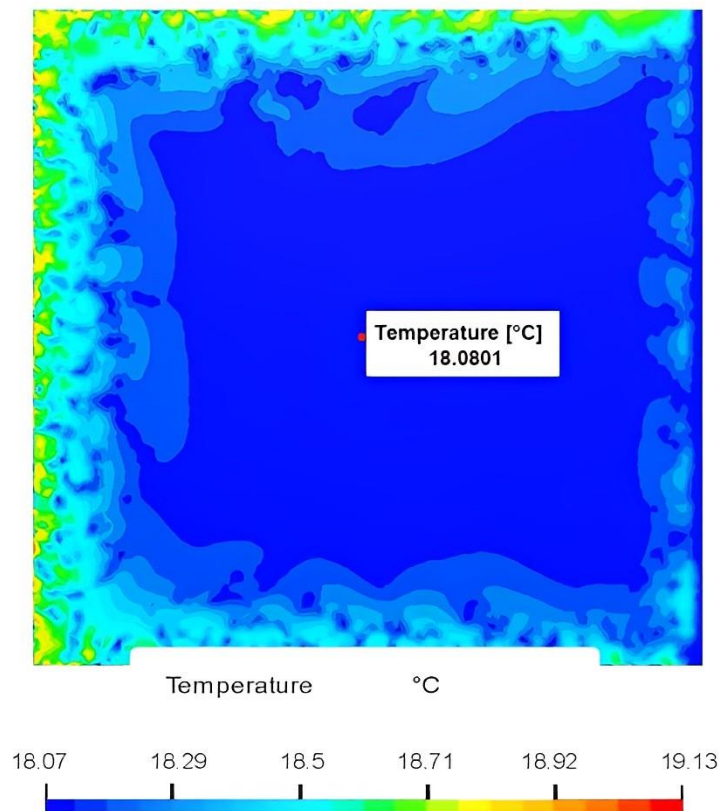


Figure A6. Simulation of TTI filled with R134a using the k-omega STT turbulence model.

References

1. International Energy Agency. *World Energy Outlook 2022*; IEA: Paris, France, 2022; pp. 288–289.
2. Fokaidis, P.A.; Kalogirou, S.A. Application of infrared thermography for the determination of the overall heat transfer coefficient (U-Value) in building envelopes. *Appl. Energy* **2011**, *88*, 4358–4365. [[CrossRef](#)]
3. Lucchi, E. Applications of the infrared thermography in the energy audit of buildings: A review. *Renew. Sustain. Energy Rev.* **2018**, *82*, 3077–3090. [[CrossRef](#)]
4. Youcef, M.L.; Feuillet, V.; Ibos, L.; Candau, Y.; Balcon, P.; Filloux, A. In situ quantitative diagnosis of insulated building walls using passive infrared thermography. In Proceedings of the 11th International Conference on Quantitative InfraRed Thermography, Naples, Italy, 11–14 June 2012. [[CrossRef](#)]
5. Barbi, S.; Barbieri, F.; Marinelli, S.; Rimini, B.; Merchiori, S.; Bottarelli, M.; Montorsi, M. Phase Change Material Evolution in Thermal Energy Storage Systems for the Building Sector, with a Focus on Ground-Coupled Heat Pumps. *Polymers* **2022**, *14*, 620. [[CrossRef](#)] [[PubMed](#)]
6. Sun, Y.; Wilson, R.; Wu, Y. A Review of Transparent Insulation Material (TIM) for building energy saving and daylight comfort. *Appl. Energy* **2018**, *226*, 713–729. [[CrossRef](#)]
7. Paneri, A.; Wong, I.L.; Burek, S. Transparent insulation materials: An overview on past, present and future developments. *Sol. Energy* **2019**, *184*, 59–83. [[CrossRef](#)]
8. Bao, Y.; Guo, R.; Kang, Q.; Liu, C.; Zhang, W.; Zhu, Q. Transparent, thermal insulation and UV-shielding coating for energy efficient glass window. *Ceram. Int.* **2021**, *47*, 24597–24606. [[CrossRef](#)]
9. Manz, H.; Egolf, P.W.; Suter, P.; Goetzberger, A. TIM-PCM external wall system for solar space heating and daylighting. *Sol. Energy* **1997**, *61*, 6, 369–379. [[CrossRef](#)]
10. Kalnæs, S.E.; Jelle, B.P. Phase change materials and products for building applications: A state-of-the-art review and future research opportunities. *Energy Build.* **2015**, *94*, 150–176. [[CrossRef](#)]
11. Li, D.; Zhang, C.; Li, Q.; Liu, C.; Arici, M.; Wu, Y. Thermal performance evaluation of glass window combining silica aerogels and phase change materials for cold climate of China. *Appl. Therm. Eng.* **2019**, *165*, 114547. [[CrossRef](#)]

12. Torres-Rodríguez, A.; Morillón-Gálvez, D.; Aldama-Ávalos, D.; Hernández-Gómez, V.H.; Kerdan, I.G. Thermal performance evaluation of a passive building wall with CO₂-filled transparent thermal insulation and paraffin-based PCM. *Sol. Energy* **2020**, *205*, 1–11. [[CrossRef](#)]
13. Rangel, C.G.; Rivera-Solorio, C.; Gijón-Rivera, M.; Mousavi, S. The effect on thermal comfort and heat transfer in naturally ventilated. *Energy Build.* **2022**, *274*, 112453. [[CrossRef](#)]
14. Souayfane, F.; Biwole, P.H.; Fardoun, F. Thermal behavior of a translucent superinsulated latent heat energy storage wall in summertime. *Appl. Energy* **2018**, *217*, 390–408. [[CrossRef](#)]
15. Le Neindre, B.; Garrabos, Y.; Tufeu, R. Thermal conductivity of dense noble gases. *Phys. A Stat. Mech. Its Appl.* **1989**, *156*, 512–521. [[CrossRef](#)]
16. Laesecke, A.; Perkins, R.; de Castro, C.N. Thermal conductivity of R134a. *Fluid Phase Equilibria* **1992**, *80*, 263–274. [[CrossRef](#)]
17. Souayfane, F.; Biwole, P.H.; Fardoun, F.; Achard, P. Energy performance and economic analysis of a TIM-PCM wall under different climates. *Energy* **2019**, *169*, 1274–1291. [[CrossRef](#)]
18. Okochi, G.S.; Yao, Y. A review of recent developments and technological advancements of variable-air-volume (VAV) air-conditioning systems. *Renew. Sustain. Energy Rev.* **2016**, *59*, 784–817. [[CrossRef](#)]
19. Envirotrolsgroup. LM24(-T) US BELIMO. Available online: https://r.search.yahoo.com/_ylt=AwrFBFddIXjzjsCy11U04lQ;_ylu=Y29sbwNiZjEEcG9zAzEEdnRpZAMEc2VjA3Ny/RV=2/RE=1669108189/RO=10/RU=http%3a%2f%2fwwww.envirotrolsgroup.com%2fBelimo%2fGeneralDamperActuators%2fLMSeries%2fLM24-3-5P0-T_1_1.pdf/RK=2/RS=5JezmoXFfRxb2msexXeybcYp7Fc (accessed on 21 November 2022).
20. Siemens Industry. GDE 131.1U. Available online: <https://www.kele.com/product/actuators-and-dampers/non-spring-return/siemens-industry/gde131.1u> (accessed on 21 November 2022).
21. Ali, A.H.; Ibrahim, S.I.; Jawad, Q.A.; Jawad, R.S.; Chaichan, M.T. Effect of nanomaterial addition on the thermophysical properties of Iraqi paraffin wax. *Case Stud. Therm. Eng.* **2019**, *15*, 100537. [[CrossRef](#)]
22. Nižetić, S.; Arıcı, M.; Bilgin, F.; Grubišić-Čabo, F. Investigation of pork fat as potential novel phase change material for passive cooling applications in photovoltaics. *J. Clean. Prod.* **2018**, *170*, 1006. [[CrossRef](#)]
23. Rathore, P.K.S.; Shukla, S.K. Enhanced thermophysical properties of organic PCM through shape stabilization for thermal energy storage in buildings: A state of the art review. *Energy Build.* **2021**, *236*, 110799. [[CrossRef](#)]
24. Honeywell. Genetron Properties Suite v 1.4.1. Available online: <https://www.honeywell-refrigerants.com/europe/genetron-properties-suite/> (accessed on 21 November 2022).
25. ANSI/ASHRAE Standard 34-2019. Designation and Safety Classification of Refrigerants. Available online: https://ashrae.iwrapper.com/ASHRAE_PREVIEW_ONLY_STANDARDS/STD_34_2019 (accessed on 28 November 2022).
26. OPAQUE 3. Available online: <https://www.sbse.org/resources/opaque> (accessed on 18 December 2022).
27. Churchill, S.W.; Chu, H.H. Correlating equations for laminar and turbulent free convection from a horizontal cylinder. *Int. J. Heat Mass Transf.* **1975**, *18*, 1049–1053. [[CrossRef](#)]
28. Soltis, D.; Jackson, J.E. Physical Properties of Materials. In *ASHRAE Handbook-Fundamentals*; Kennedy, H.E., Ed.; ASHRAE Research: Peachtree Corners, GA, USA, 2021; pp. 33.1–33.4.
29. Soltis, D.; Jackson, J.E. Thermal properties of foods. In *ASHRAE Refrigeration*; Kennedy, H.E., Ed.; ASHRAE Research: Peachtree Corners, GA, USA, 2018; pp. 19.1–19.31.
30. Propiedades del Acrílico. Available online: http://plasco.com.mx/upload/productos/6_318.pdf (accessed on 22 December 2022).
31. Cengel, Y.A. *Transferencia de Calor*, 2nd ed.; Mc Graw Hill: Distrito Federal, México, 2004; p. 736.
32. Onshape Product Development Platform. Available online: <https://www.onshape.com/en/> (accessed on 10 February 2022).
33. Simulation Software Engineering in the Cloud I SimScale. Available online: <https://www.simscale.com/> (accessed on 2 April 2022).
34. ParaView 5.6.2. Available online: <https://www.paraview.org/> (accessed on 20 April 2022).
35. Calculation of Thermal Mass according to EN ISO 13786. Available online: <https://www.htflux.com/en/freecalculatointoolfor-thermalmassofbuildingcomponentsiso13786/> (accessed on 4 April 2023).

Disclaimer/Publisher's Note: The statements, opinions and data contained in all publications are solely those of the individual author(s) and contributor(s) and not of MDPI and/or the editor(s). MDPI and/or the editor(s) disclaim responsibility for any injury to people or property resulting from any ideas, methods, instructions or products referred to in the content.